ABSTRACT

Title of Thesis:	DIRECT LASER FABRICATION OF DIFFRACTION GRATINGS ON POLYMER THIN FILMS AND WAVEGUIDES
	Glenn D Hutchinson, Master of Science, 2005
Thesis Directed By:	Professor Chi H. Lee, Department of Electrical and Computer Engineering

With the increasing interest in polymer integrated optical devices, techniques for fabrication of efficient polymer diffraction gratings are of critical importance to aid in coupling of light into and out of polymer waveguides. We have been developing direct laser fabrication techniques for diffraction gratings and standard photo-lithographic techniques for polymer waveguides. The investigation of the laser fabrication is carried out using a 193 nm ArF excimer laser. Symmetric and blazed gratings were fabricated on polymer thin films and characterized. Diffraction efficiencies into a single order as high as 79% have been observed. In addition, gratings were fabricated on multi-mode polymer dispensed waveguides for use as input couplers and on single mode photo-lithographically fabricated polymer waveguides for use as output couplers. Output coupling efficiencies of 32% have been observed.

DIRECT LASER FABRICATION OF DIFFRACTION GRATINGS ON POLYMER THIN FILMS AND WAVEGUIDES

By

Glenn David Hutchinson

Thesis submitted to the Faculty of the Graduate School of the
University of Maryland, College Park, in partial fulfillment
of the requirements for the degree of
Master of Science
2005

Advisory Committee:
Professor Chi H. Lee, Chair
Professor Julius Goldhar
Doctor Warren Herman

Dedication

To my family, friends and colleagues.

Acknowledgements

I would like to first thank my many advisors, Dr. Chi Lee, Dr. Julius Goldhar and Dr. Warren Herman for their support over the last 2 years. In addition to funding my research they provided me with the framework and guidance necessary to complete this work.

I would like to thank Dr. Yongzhang Leng who oversaw my early work with the laser fabrication project. I would also like to thank Younggu Kim for fabricating my single mode polymer waveguides. Finally, I would like to acknowledge and thank Victor Yun and Lisa Lucas for their efforts.

Table of Contents

Chapter 1: Introduction

1.1 Motivation

With the increasing interest in polymer integrated optical devices, techniques for fabrication of efficient polymer diffraction gratings are of critical importance to aid in coupling of light into and out of polymer waveguides [1-3]. We have been developing direct laser fabrication techniques for diffraction gratings and polymer waveguides [4]. Laser fabrication offers tremendous cost and time savings over conventionally lithographic techniques mainly because there is no need for the design and fabrication of a mask [5]. However there are trades off, namely with resolution and scalability. Modern lithographic techniques can reliably produce feature sizes below 1 μm [6], and, while we have produced gratings with periods below 1 μm, limitations due to optics and the spectrum of the laser being used, have limited the total grating width. This limitation will be discussed in 4.2.3. In addition laser fabrication is not easily scalable for multi-device fabrication as each feature that is fabricated requires movement and realignment of the sample. However, despite these limitations, laser fabrication still offers rapid prototyping and a significant cost and time savings as compared to conventional lithography.

1.2 Project goals

The ongoing work with laser fabrication at the Laboratory for Physical Sciences has two primary goals. The first is the direct laser fabrication of waveguides in thin polymer films and the second, which is the primary topic of this thesis, is the

direct laser fabrication of diffraction gratings on polymer waveguides to be used for coupling of light into and out of the waveguides.

1.2.1 Waveguide fabrication

Waveguide fabrication is accomplished by ablating a polymer film to create parallel channels on a two or three layer polymer structure that is spin coated onto a Si Substrate. The channels are carved into the structure by focusing a 193nm ArF Excimer laser onto the polymer and moving the device via a high precision stage [7].

The process starts by selecting two polymers with different refractive indices for waveguide fabrication. Commonly used polymers for this work have involved Benzocyclobutene™ (BCB, Dow chemical) and Pyralin™ (PI, DuPont). BCB has an index of refraction of 1.56 at 1.55 μm and is a suitable choice as a cladding material for use in a waveguide utilizing PI as a core material which has an index of 1.59 at 1550 nm. BCB is spin coated onto a Si substrate followed by the further spin coating of a PI layer. In addition, another BCB layer can be fabricated on top of the core PI layer if a symmetric structure is desired. An excimer laser is then used to ablate two parallel channels in the BCB/PI stack. The end result is a waveguide structure which utilizes air as the cladding layer on the sides (Fig. (1)). Waveguides with losses on the order of 1.3 dB/cm have been fabricated.

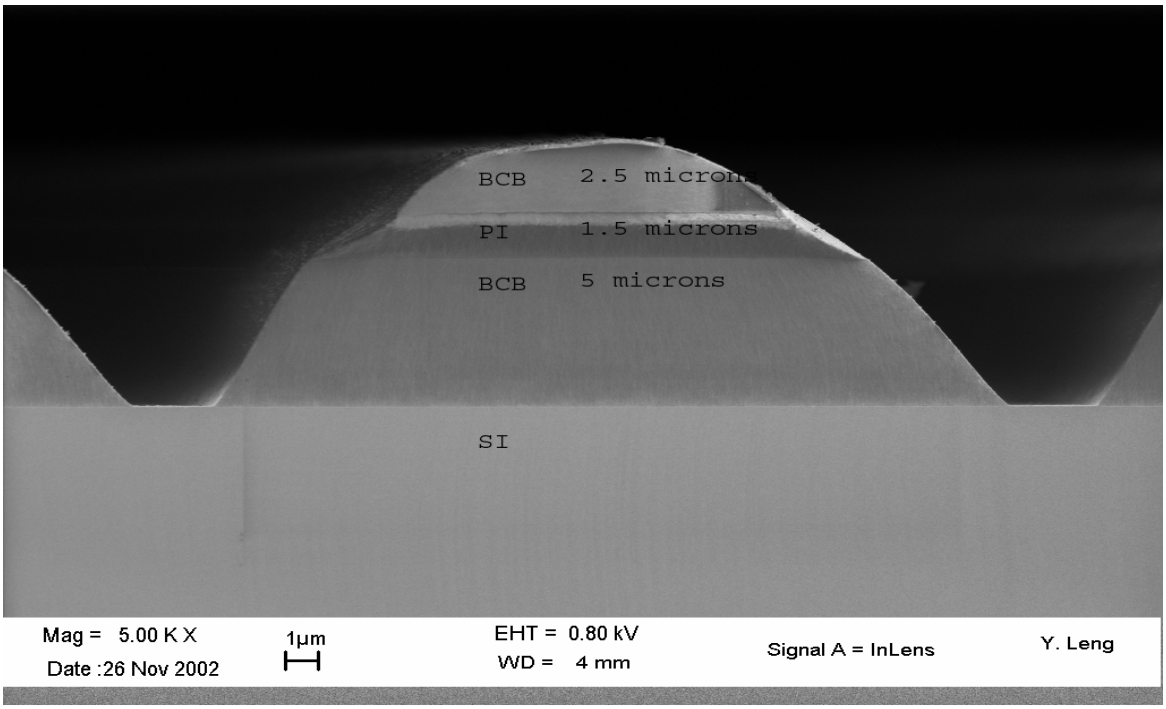

Figure 1 SEM cross section of laser fabricated waveguide.

1.2.2 Grating fabrication

The investigation of the grating fabrication is carried out using a 193 nm ArF excimer laser with a pulse width of 20 ns. Grating structures with different periods are fabricated on polymer thin films by interference of two beams created by a phase mask as shown in Fig. (2). The zeroth and higher orders are suppressed so that only the first order beams are allowed to interfere. A quartz triplet lens is then used to focus the beams together on the sample. In addition, by changing the angle of the sample, various asymmetric or blazed grating shapes can be created [4].

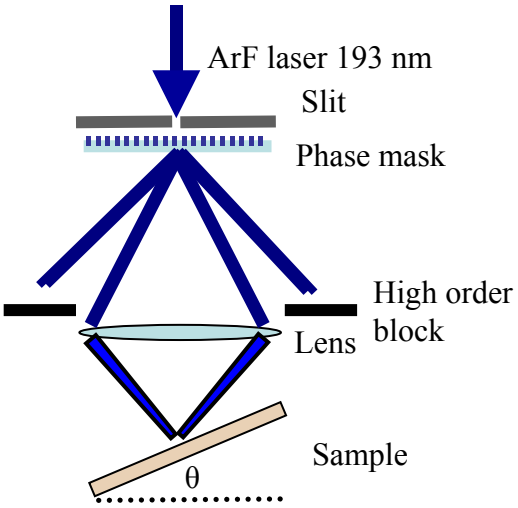

Figure 2 Schematic of grating fabrication experiment

Gratings have been fabricated on multimode polymer dispensed waveguides to serve as input couplers as well as on single-mode lithographically fabricated polymer waveguides to serve as output couplers. Output coupling efficiencies of up to 32% have been measured from the single mode waveguides excited by a 1550 nm source.

Similar grating fabrication techniques utilizing transmission optics and a phase mask have been carried out by Chen et al [8]. However their work was done on $LiNbO_3$ as opposed to polymers. In addition instead of using a lens to focus the beams, a Schwarzschild objective was used. Some work has been done with our project utilizing a Schwarzschild objective, however the majority of our work has been done with a lens due to constraints with sample placement while fabricating blazed gratings.

In addition, other groups have explored methods that involve direct imaging of the phase mask on various materials [9] and on polymers [10,11]. The main drawback is that a new phase mask must be created to create gratings with different

periods. This method however, would still offer advantages over conventional lithography since it could all be done outside of a clean room. This method was originally developed [9] and used for the etching of gratings on optical fibers which are not readily compatible with existing lithographic techniques.

Another method utilizing a Michelson interferometer has also been demonstrated [12,13]. In this setup, a laser beam is split into two beams which are reflected back to each other via two mirrors and interfere at the sample.

1.3 Thesis organization

The remainder of this thesis is organized into four additional chapters. Chapter two will give an overview of diffraction theory which is necessary to understand the grating fabrication process and is also important for the design of input/output grating couplers. The simple yet extremely important grating equation will be derived, and in addition I will derive the conditions necessary to excite a guided mode in a waveguide due to diffraction of incoming light by a grating.

Chapter three will discuss the primary polymer (BCB) used for my work. This chapter will discuss our primary reasons for choosing this polymer as well as the process involved in creating a polymer film from the polymer resin. Chapter four will give a detailed description of the laser fabrication system. The equipment used as well as the process involved will be discussed.

Chapter five will discuss the experimental and theoretical characterization of the gratings on various structures. Characterization includes transmission measurements and theoretical calculations of gratings fabricated on a BCB layer which was spin coated onto a glass slide. I will also demonstrate and present a simple

model of the input coupling of a HeNe source into a multi-mode dispensed polymer waveguide. Finally, work involving the output coupling efficiency of 1550 nm light from a single mode waveguide via the gratings will be presented and analyzed. Chapter six will conclude this thesis with a summary of the work done and suggested future work.

Chapter 2: Diffraction grating theory

2.1 Overview

Diffraction phenomena can be observed by partially obstructing a point source with a screen. By varying the size of the opening in the screen a periodic fluctuation in the intensity will be observed. Diffraction theory can best be described with the application of Huygens Principle coupled with the principle of interference [14] which was first done by Fresnel. Huygens principle states that any point on a wave-front may be considered a secondary disturbance which gives rise to another spherical wave or wavelet. The wave-front at any later time may be regarded as the envelope of these wavelets. Fresnel took this idea and then postulated that the secondary wavelets could mutually interfere [14] thus giving rise to intensity fluctuations if different wavelets on the wave-front were blocked. Kirchoff later put this on a sound mathematical basis with the derivation of the Fresnel-Kirchoff diffraction formula [14,15]:

$$U(P) = -\frac{i}{2\lambda}\int_S \frac{U_0 e^{ik(r'+r)}}{r'r}[\cos(\theta') + \cos(\theta)]dS \,. \qquad (1)$$

Eq. (1) gives the disturbance at P due to a point source P', located a distance r' from an element *dS* of the surface of integration (the aperture). Here the integral is over the area of the aperture, and U_0 is the aperture distribution or transfer function. Specifically, U_0 represents the total amplitude and phase transformation that an incoming wave will undergo. As an example, for a slit which is assumed to be infinitely thin, an incoming wave would undergo an amplitude change. At the open

portion of the slit U_0 is equal to unity; U_0 is zero everywhere else. r is the distance of the observation point from an element *dS* of the aperture and $\theta'(\theta)$ is the angle that r' (r) makes with respect to the normal of the surface, see Fig. (3).

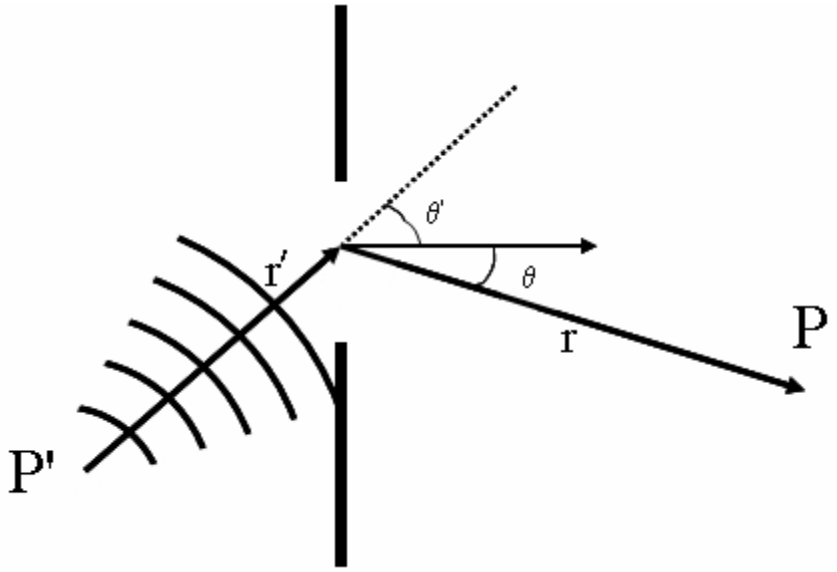

Figure 3

Some approximations can be made to simplify Eq. (1). Namely if r' and r are much larger than the dimensions of the aperture then they will not vary much with respect to the surface integral and so we can let $r' \to r_0'$ and $r \to r_0$ in the denominator. We define r_0' and r_0 as the distance from the center of the aperture to the source and observation point respectively. In addition θ' and θ will not vary much over the aperture. Letting $\theta' \to \theta_0'$ and $\theta \to \theta_0$ we can then pull the $[\cos(\theta_0') + \cos(\theta_0)]$ term out of the integral. The integral now takes the form:

$$U(P) = -\frac{i[\cos(\theta_0') + \cos(\theta_0)]}{2\lambda r_0' r_0} \int_S U_0 e^{ik(r'+r)} dS \,. \qquad (2)$$

2.2 Fraunhofer diffraction limit

Up to this point we have not considered the shape of the aperture. In fact Eq. (2) is suitable for determining the diffraction of a point source due to an arbitrarily shaped two dimensional surface provided the source and observation point are sufficiently far as compared to the dimensions of the aperture. However to simplify matters we will treat the aperture as a slit (ignore width) which is small in height as compared to the locations of the source and observation. We now define a new coordinate system and set x and y to be parallel and perpendicular to the aperture respectively and place the origin at the center of the aperture. We will next consider the aperture to be one dimensional and replace the surface integral with a line integral over x,

$$\int_S dS \to \int_l dx \,. \tag{3}$$

Defining (x_0', y_0') and (x_0, y_0) as the position of P' and P respectively and x as the location along the aperture of the differential length dl we can rewrite r_0', r_0, r' and r as :

$$\begin{aligned} r_0'^2 &= x_0'^2 + y_0'^2, \\ r_0^{\,2} &= x_0^{\,2} + y_0^{\,2}, \end{aligned} \tag{4}$$

$$\begin{aligned} r'^2 &= (x_0' - x)^2 + y_0'^2, \\ r^2 &= (x_0 - x)^2 + y_0^{\,2}. \end{aligned} \tag{5}$$

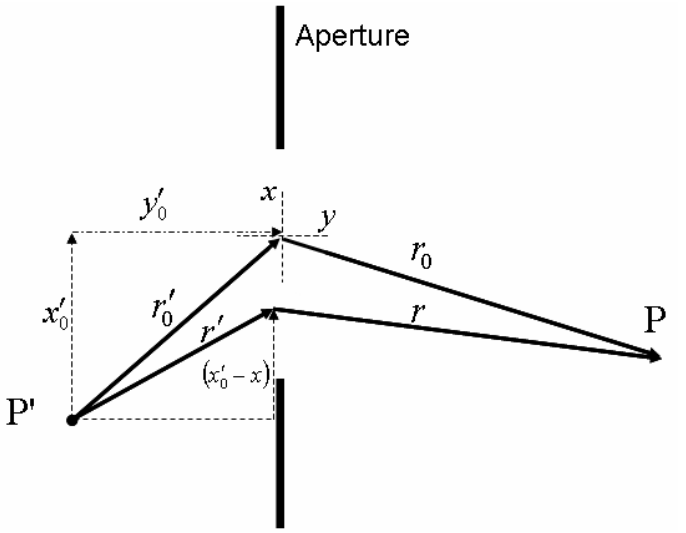

Figure 4 New coordinate system

The associated coordinate transformation from the continuous variables $r, r' \to x$ is depicted in Fig. (4). We can rearrange these two equations and write r'^2 and r^2 in terms of $r_0'^2$ and $r_0{}^2$ respectively:

$$\begin{aligned} r'^2 &= r_0'^2 - 2x_0'x + x^2, \\ r^2 &= r_0{}^2 - 2x_0x + x^2. \end{aligned} \tag{6}$$

If we assume that the dimension of the aperture is small with respect to $r_0'^2$ and $r_0{}^2$ then we can expand r'^2 and r^2 as a power series in x/r_0' and x/r_0 :

$$\begin{aligned} r' &\approx r_0' - \frac{x_0'x}{r_0'} + \frac{x^2}{2r_0'} - \frac{(x_0'x)^2}{2r_0'^3} - \cdots , \\ r &\approx r_0 - \frac{x_0x}{r_0} + \frac{x^2}{2r_0} - \frac{(x_0x)^2}{2r_0{}^3} - \cdots . \end{aligned} \tag{7}$$

Substituting back into (2),

$$U(P) = -\frac{i[\cos(\theta_0') + \cos(\theta_0)]e^{ik(r_0' + r_0)}}{2\lambda r_0' r_0} \int_x U_0 e^{ikf(x)} dx , \tag{8}$$

where

$$f(x)=\left(-\frac{x_0'}{r_0'}-\frac{x_0}{r_0}\right)x+\frac{x^2}{2r_0}\left(1-\frac{{x_0}^2}{{r_0}^2}\right)+\frac{x^2}{2r_0'}\left(1-\frac{{x_0'}^2}{{r_0'}^2}\right). \tag{9}$$

Looking at the terms that are quadratic in x^2, it should be obvious that they can be neglected provided that the terms do not make a significant impact in the exponent, i.e.

$$k\left|\frac{x^2}{2r_0}\left(1-\frac{{x_0}^2}{{r_0}^2}\right)+\frac{x^2}{2r_0'}\left(1-\frac{{x_0'}^2}{{r_0'}^2}\right)\right|<<2\pi\,. \tag{10}$$

Because $\frac{{x_0}^2}{{r_0}^2}$ and $\frac{{x_0'}^2}{{r_0'}^2}$ are always ≤ 1, the following conditions must be satisfied in order to neglect the higher order terms.

$$\begin{aligned}\left|r_0'\right| &>> \frac{{x^2}_{\max}}{\lambda}\ ,\\ \left|r_0\right| &>> \frac{{x^2}_{\max}}{\lambda}\ .\end{aligned} \tag{11}$$

Noting that $-\frac{x_0'}{r_0'}$ and $\frac{x_0}{r_0}$ can be rewritten as $\sin(\theta_0')$ and $\sin(\theta_0)$ respectively, Eq. (8) becomes

$$U(P)=-\frac{i[\cos(\theta_0')+\cos(\theta_0)]e^{ik(r_0'+r_0)}}{2\lambda r_0' r_0}\int_x U_0 e^{ik(\sin(\theta_0')-\sin(\theta_0))x}dx\,. \tag{12}$$

In general, if higher order terms can be neglected the phenomenon is referred to as Fraunhofer diffraction. If the quadratic terms cannot be neglected then it is referred to as Fresnel diffraction. Simply stated this means that in Fraunhofer diffraction the source and observation points are sufficiently far away with respect to

the wavelength, that one may consider the incident and diffracted waves to be plane waves. However, if the wave front curvature is not negligible then higher order terms cannot be neglected and we have Fresnel diffraction. This is illustrated in Fig. (5).

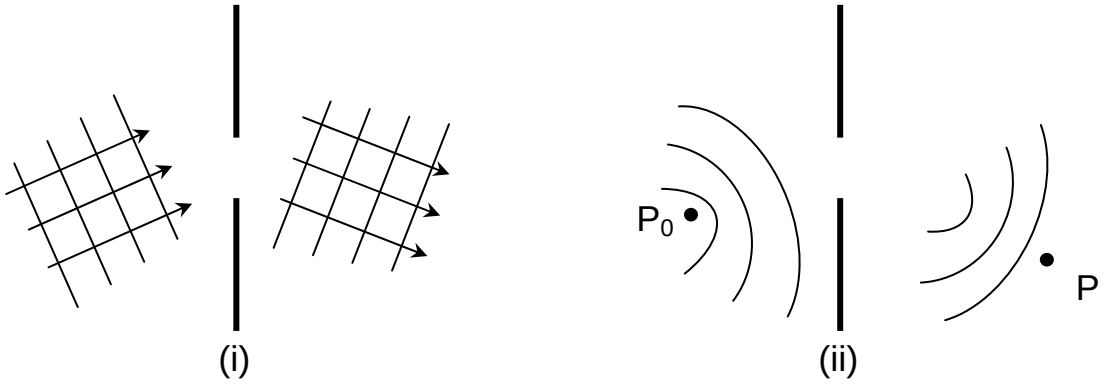

Figure 5 Diffraction limits (i) Fraunhofer (ii) Fresnel

2.3 Diffraction by a periodic array of elements

If we now consider the case of n periodic slits in the Fraunhofer limit we let

$$\begin{aligned} x &\to x + nd \quad , \\ dx &\to dx \qquad . \end{aligned} \tag{13}$$

where n is the index of the nth element and d is the distance between elements. We then sum over all elements. Eq. (8) becomes

$$\begin{aligned} U(P) &= -\frac{i[\cos(\theta_0') + \cos(\theta_0)]e^{ik(r_0' + r_0)}}{2\lambda r_0' r_0} \sum_n \int_x U_0 e^{ik(\sin(\theta_0') - \sin(\theta_0))(x+nd)} dx \\ &= -\frac{i[\cos(\theta_0') + \cos(\theta_0)]e^{ik(r_0' + r_0)}}{2\lambda r_0' r_0} \sum_n e^{iknd(\sin(\theta_0') - \sin(\theta_0))} \int_x U_0 e^{ik(\sin(\theta_0') - \sin(\theta_0))x} dx \quad . \end{aligned} \tag{14}$$

Designating $U_0(P)$ as the field disturbance due a single element, (15) takes the form

$$U(P) = U_0(P) \sum_n e^{iknd(\sin(\theta_0') - \sin(\theta_0))} \quad , \tag{15}$$

where

$$U_0(P) = -\frac{i[\cos(\theta_0') + \cos(\theta_0)]e^{ik(r_0' + r_0)}}{2\lambda r_0' r_0}\int_x U_0 e^{ik(\sin(\theta_0') - \sin(\theta_0))x} dx \quad . \tag{16}$$

The geometric sum in (15) converges exactly and we have

$$U(P) = U_0(P)\frac{1 - e^{-iNkd(\sin(\theta_0') - \sin(\theta_0))}}{1 - e^{-ikd(\sin(\theta_0') - \sin(\theta_0))}} \quad . \tag{17}$$

Taking the magnitude squared of (17) yields the intensity distribution of the scattered light.

$$\begin{aligned} I(P) &= |U_0(P)|^2 \left| \frac{1 - e^{-iNkd(\sin\theta_0' - \sin\theta_0)}}{1 - e^{-ikd(\sin\theta_0' - \sin\theta_0)}} \right|^2 \\ &= \frac{1 - \cos[Nkd(\sin\theta_0' - \sin\theta_0)]}{1 - \cos[kd(\sin\theta_0' - \sin\theta_0)]} I_0(P) \\ &= \frac{\sin^2\left[\frac{Nkd}{2}(\sin\theta_0' - \sin\theta_0)\right]}{\sin^2\left[\frac{kd}{2}(\sin\theta_0' - \sin\theta_0)\right]} I_0(P) \quad , \end{aligned} \tag{18}$$

where $I_0(P) = |U_0(P)|^2$.

We now evaluate $U_0(P)$ for a slit aperture of height a. Since the transfer function of a slit is unity over the area of the slit, $U_0 \to 1$ and the integral will be over the length of the slit.

$$\int_{-a}^{a} e^{ik(\sin\theta_0' - \sin\theta_0)x} dx = 2\frac{\sin[k(\sin\theta_0' - \sin\theta_0)a]}{k(\sin\theta_0' - \sin\theta_0)} \quad . \tag{19}$$

Evaluating $I_0(P)$ we have

$$I_0(P) = I_0\left[\frac{\sin(k(\sin\theta_0' - \sin\theta_0)a)}{k(\sin\theta_0' - \sin\theta_0)}\right]^2 \quad , \tag{20}$$

where

$$I_0 = \left| -\frac{i[\cos(\theta_0') + \cos(\theta_0)]e^{ik(r_0'+r_0)}}{\lambda r_0' r_0} \right|^2 \quad . \tag{21}$$

Substituting (20) into (18) we have

$$I(P) = I_0 \left[\frac{\sin\left(k\left(\sin\theta_0' - \sin\theta_0\right)a\right)}{k\left(\sin\theta_0' - \sin\theta_0\right)} \right]^2 \left[\frac{\sin\left(\frac{Nkd}{2}\left(\sin\theta_0' - \sin\theta_0\right)\right)}{\sin\left(\frac{kd}{2}\left(\sin\theta_0' - \sin\theta_0\right)\right)} \right]^2 \quad . \tag{22}$$

The function represents the intensity distribution of light diffracted from N parallel slits. The $\left[\frac{\sin(N\beta)}{\sin(\beta)}\right]^2$ term is just the normalized interference function while the $\left[\frac{\sin(\alpha x)}{\alpha}\right]^2$ term is the normalized intensity function of a slit. This equates to the modulation of a periodic interference function by the intensity of a slit as illustrated in Fig. (6).

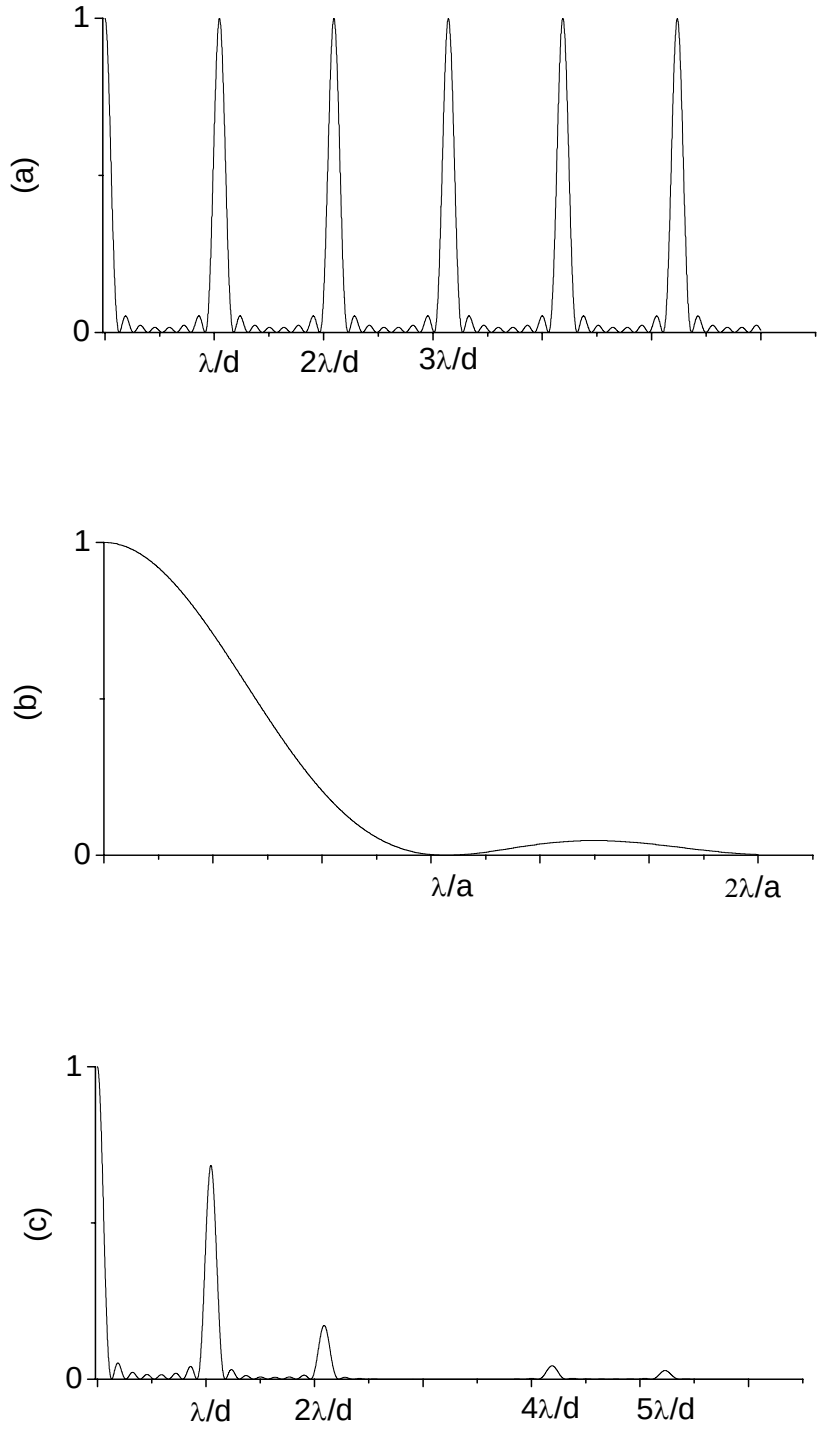

Figure 6 (a) Normalized interference function
(b) Normalized intensity distribution of a slit
(c) Diffraction pattern due to a periodic array of slits

2.4 The grating equation

The function $\frac{\sin^2(N\alpha)}{\sin^2(\alpha)}$ has maxima of height N^2 whenever α is a multiple of π. Setting the argument of the sine function in the denominator of Eq. (18) equal to $m\pi$ we have

$$\frac{kd}{2}(\sin\theta_0' - \sin\theta_0) = m\pi \quad . \tag{23}$$

Rewriting k as $\frac{2\pi}{\lambda}$ and rearranging (23) we have

$$\sin\theta_0' - \sin\theta_0 = \frac{m\lambda}{d} \qquad (m = 0,\pm1,\pm2,...) \quad . \tag{24}$$

Eq. (24) is known as the grating equation and it governs the angles at which each order (m) will diffract for a given wavelength (λ) and grating period (d). Fig. (7) is an illustration of Eq. (24) showing a beam of monochromatic light incident on a periodic structure and the associated diffracted orders and their respective angles, $\theta_0^{(m)}$.

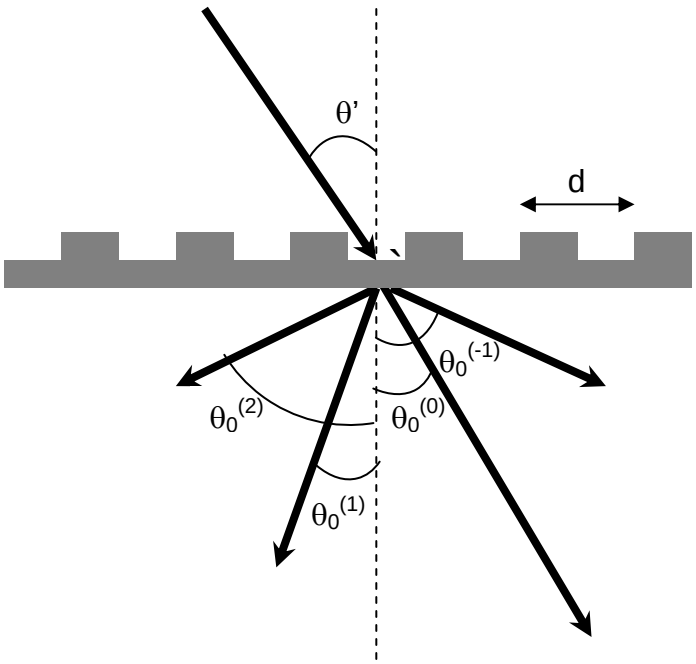

Figure 7 Diffraction of light due to incidence on a grating

Although Eq. (24) was derived for the diffraction due to a periodic array of slits, it applies to almost any periodic structure regardless of the shape of the grating or aperture. The simple theory of the location of sharp maxima should hold for any periodic modulation of a material so long as the intensity pattern of a single period varies slowly in an interval of the order λ/d [14].

2.5 The Fourier interpretation

Taking another look at Eq. (16) we see that the far field disturbance of a single diffraction element is simply the Fourier transform of the diffraction elements transfer function, U_0 of the aperture. The Fourier transform converts the transfer function from the domain of the aperture (x) to the domain of $\frac{\sin\theta_0' - \sin\theta_0}{\lambda}$. This approach

will be used later to perform a numerical calculation of the diffraction pattern for various grating shapes.

2.6 Input coupling into waveguides

Our primary goal of grating fabrication is for the input coupling of light into waveguides. One can solve for the β's which are the z components of the wave vector k of a guided mode. Then if a free space wave is diffracted into a waveguide via the gratings and one of the diffracted orders has $k_z = \beta$ the wave will propagate in the guide [16,17].

In the previous derivations we failed to consider if the region in which the light was being diffracted had a different index of refraction than that of the source region. This issue can be easily accounted for by noting in Eq. (1) that the exponential in the integral should transform as

$$k(r'+r) \rightarrow k_0(n'r'+nr) \quad , \tag{25}$$

where n' and n are the indices of refraction for the source and observation regions respectively. Carrying this change through, Eq. (23) becomes

$$\frac{k_0 d}{2}\left(n'\sin\theta_0' - n\sin\theta_0\right) = m\pi \quad . \tag{26}$$

Rearranging gives

$$k_0 n'\sin\theta_0' - k_0 n\sin\theta_0 = \frac{2\pi m}{d} \quad . \tag{27}$$

Now the wave vector of an incoming plane wave can be written as

$$\vec{k} = \vec{a}_T k_0 n\cos(\theta) + \vec{a}_z k_0 n\sin(\theta) \quad . \tag{28}$$

Recognizing the first term in Eq. (27) as the z component of an incoming plane wave and the second term as the diffracted z component, we see that the grating acts to modify the incoming z component by a factor $\frac{2\pi m}{d}$, i.e.

$$k_0 n' \sin\theta_0' + \frac{2\pi m}{d}_0 = k_0 n \sin\theta$$
$$or \qquad (29)$$
$$k_z' + \frac{2\pi m}{d} = k_z \quad .$$

Note that the sign between the two terms on the left is determined by convention. I will now choose the convention that a positive diffracted order, i.e. $m = +1,+2.+3...$ will add to the z component.

If the new z component of the wave vector is equal to a β of the waveguide then the wave will be coupled into the waveguide as illustrated in Fig. (8).

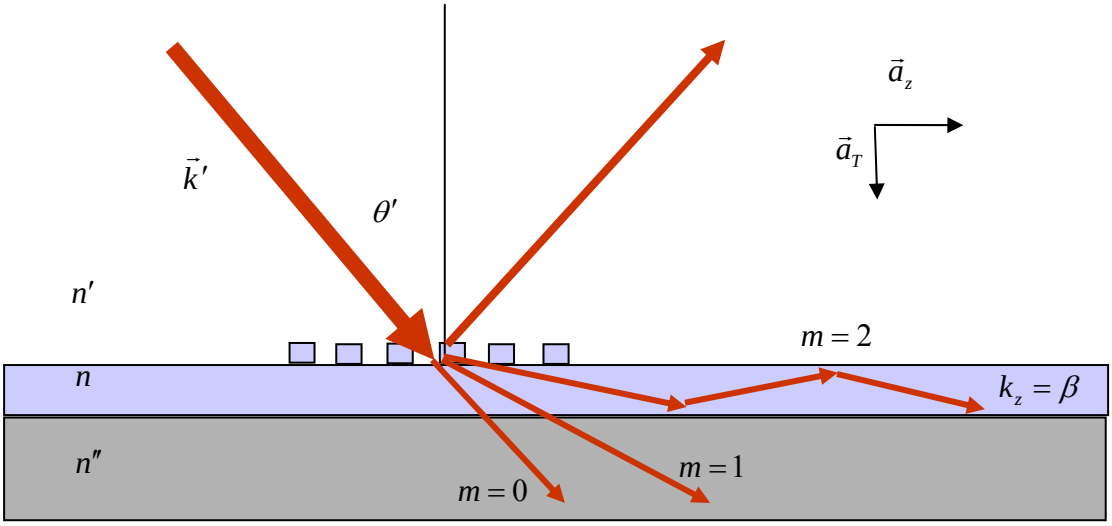

Figure 8 Input coupling with grating

Setting the right hand side of Eq. (29) equal to β we can solve for the required acceptance angle, θ' necessary for a diffracted order m to excite a guided mode β.

$$\theta' = \sin^{-1}\left[\frac{(\beta - \frac{2\pi m}{d})}{n'k_0}\right] . \qquad (30)$$

Using this theory along with the theory of guided mode wave vectors in waveguides [17] one can easily design grating structures which will couple light into a waveguide. This equation however does not guarantee that the coupling will be efficient, as the power in the other modes that are not coupled into the guide are generally scattered away. Specifically it should be obvious that it is highly desirable to have all incoming light diffracting into a single order. Tuning of the grating shape allows this by shifting the associated modulation pattern, given by Eq. (16), of the diffracted spectral orders. The issue of diffraction order tuning and efficiency will be addressed in Chapter 5 when the shape of the grating structure is considered.

Chapter 3: Cyclotene™

3.1 Origins and applications

Cyclotene™ (commonly known as BCB) is an advanced electronics Resin developed by the Dow Chemical Corporation. The resins are derived from B-staged bisbenzocyclobutene (BCB) monomers and are formulated as high-solids, low-viscosity solutions [18]. The BCB monomer chemical structure is illustrated in Fig. (9). The Cyclotene dry-etch polymers are currently being used or considered in the electronics industry for many applications including [18]:

- multichip modules
- flat panel displays (e.g., planarization layers and high aperture dielectrics)
- interlayer dielectrics (e.g., silicon and GaAs)
- micro-machines (e.g., sensors and mechanical devices)
- optical interconnects (e.g., waveguides and switches)
- stress-buffer layers (e.g., logic and memory)

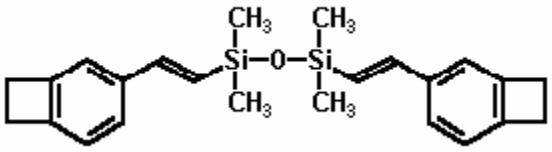

Figure 9 BCB monomer [18]

The 3022 series dry-etch polymer was chosen for our laser fabrication research primarily because the polymer exhibits high absorption at UV wavelengths (Fig. (10)) which allows for the uniform ablation of the polymer with a UV source such as an ArF laser. Pedestal single mode guides which utilized BCB as a core

guiding region have been fabricated and losses on the order of 1.5 dB/cm have been measured using the cut-back method [19]. Additionally, the polymer exhibits excellent chemical resistance, which allows for integration with conventional semiconductor processing techniques. The polymer also can be fabricated over a wide range of thickness; thin-film coatings of 1.0 to 26.0 μm are achievable in a single spin-coat application using standard IC techniques [18].

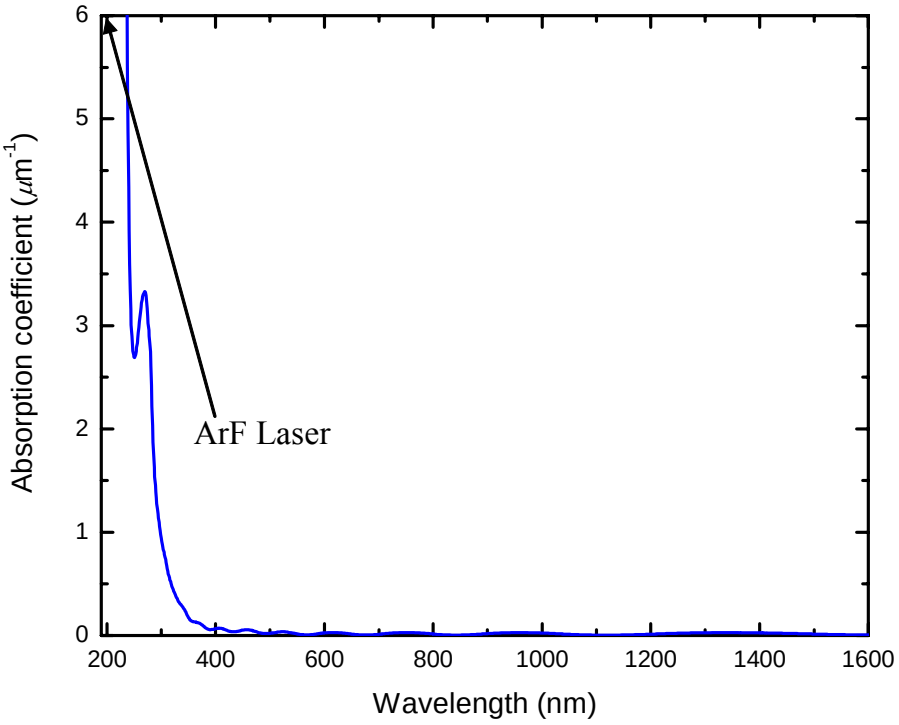

Figure 10 UV/VIS/Near IR absorption curve for BCB thin film

3.2 Fabrication techniques

BCB is spin coated onto a substrate (typically Silicon for our work) using conventional spin coating techniques. BCB resin is dispensed onto a slowing rotating (50 – 150 RPM) substrate. The substrate speed is increased (500 RPM) to spread the resin out. The speed is then increased to a rate which is appropriate to achieve the

desired coating thickness (table 1). The film is then typically cured in a convection oven in the absence of oxygen. This baking procedure typically takes 4-5 hours to complete.

Spin Speed (RPM)	**Cyclotene 3022-35**	**Cyclotene 3022-46**	**Cyclotene 3022-57**	**Cyclotene 3022-63**
1000	**2.4**	**5.8**	**15.6**	**26**
2000	**1.7**	**3.8**	**9.3**	**16**
3000	**1.3**	**3**	**7.3**	**13**
4000	**1.1**	**2.6**	**6.3**	**11**
5000	**1.0**	**2.4**	**5.7**	**9.5**

Table 1 Typical Cured Thickness (μm) of Film

Chapter 4: Laser Fabrication of Gratings

4.1 The laser fabrication system

4.1.1 System layout

At the heart of the laser fabrication system is an ArF (193 nm) laser and three high precision translation stages and associated controllers (X, Y and Z). Light from the laser is manipulated using a variety of optical components and focused on the sample, which is mounted on the stage. Through the movement of the XY stage any portion of the sample can be addressed and ablated. Adjustment of the Z stage allows fine tuning of the focus of the laser. Fig. (11) shows a schematic of the base laser fabrication system. The stage movement and triggering of the laser are controlled with a computer. A vacuum chuck is mounted to the XY stage and holds the sample during fabrication. With this base configuration, simple ablation of material can occur. The fabrication of gratings is accomplished through additional manipulation of the source which will be discussed later.

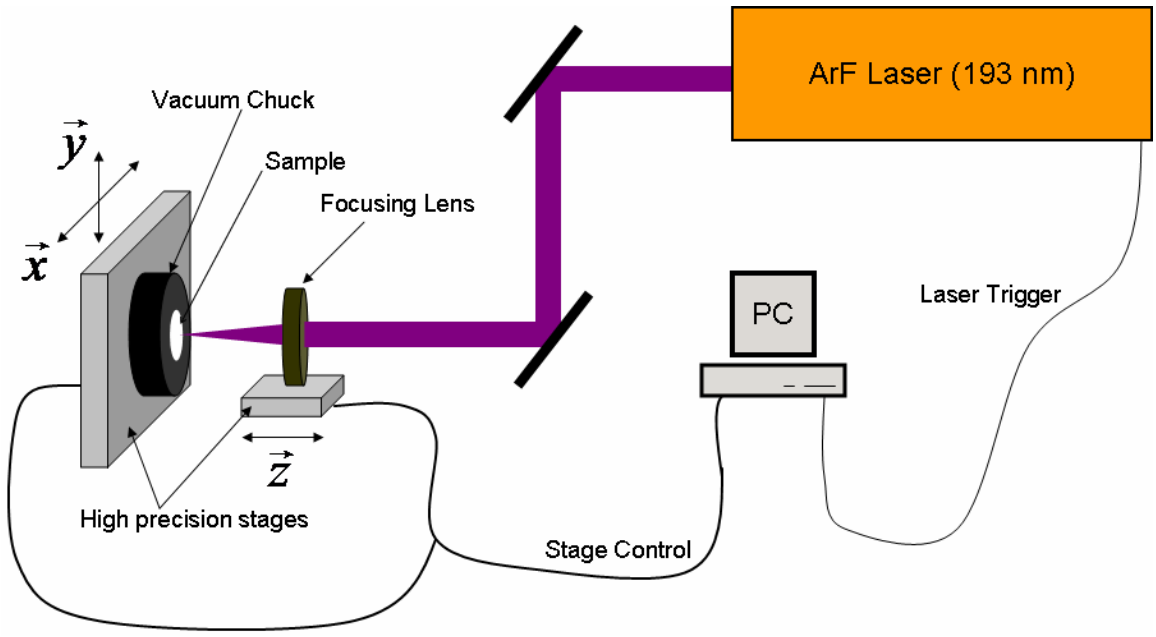

Figure 11 Laser fabrication schematic

4.1.2 High precision stage

All stages are manipulated through the use of high precision stepper motors and position encoders. The stepper motor/position encoders have sub 100 nm resolutions and can be reliably addressed down to $1/10\mu m$. The X stage has a range of 10 cm, Y stage a 5 cm range, and the Z stage has a 2.5 cm range. The stages are all connected to high precision stage controllers which can communicate with conventional PC hardware via a GPIB interface. Software has been written in both Visual Basic and Labview to facilitate the ablation of various structures in the polymer films.

4.1.3 ArF laser

The laser fabrication of the gratings in my setup was done using a LPX 210 commercial ArF laser from Lambda Physik. The laser can have power levels as high

as 400 mJ per pulse with a pulse length of ~20 ns. The laser can be pulsed up to 50 Hz via an external trigger.

4.1.4 Passive optical components for grating fabrication

Facilitation of fabrication of gratings is accomplished through the insertion of a slit and phase mask before the lens. The slit is used to select a uniform portion of the laser beam and image it on the phase mask. The laser beam before the slit is ~10 mm by 25 mm. The slit is typically on the order of a centimeter in height and a few millimeters in width. The light at the phase mask then diffracts according to the grating equation, Eq. (24).

The phase mask has a square amplitude transfer function, a period $\Lambda_{pm} = 6.67\,\mu m$ and grating depth $\sim \frac{1}{2}\frac{\lambda_{Arf}}{(n-1)} = 172\,nm$. The depth of the phase mask was chosen to be equal to half the wavelength of the laser to minimize the zeroth order beam [15]. The phase mask consists primarily of fused quartz and was patterned using standard photolithography and etched via reactive ion etching.

The zeroth diffracted order as well as orders above $+/-1$ from the illuminated phase mask are blocked. A triplet lens with a focal length of ~ 113 mm at 193 nm, is placed in front of the $+/-1$ diffracted beams. The beams recombine at the sample where they interfere to create a grating pattern on the polymer surface. The process is illustrated in Fig. (12).

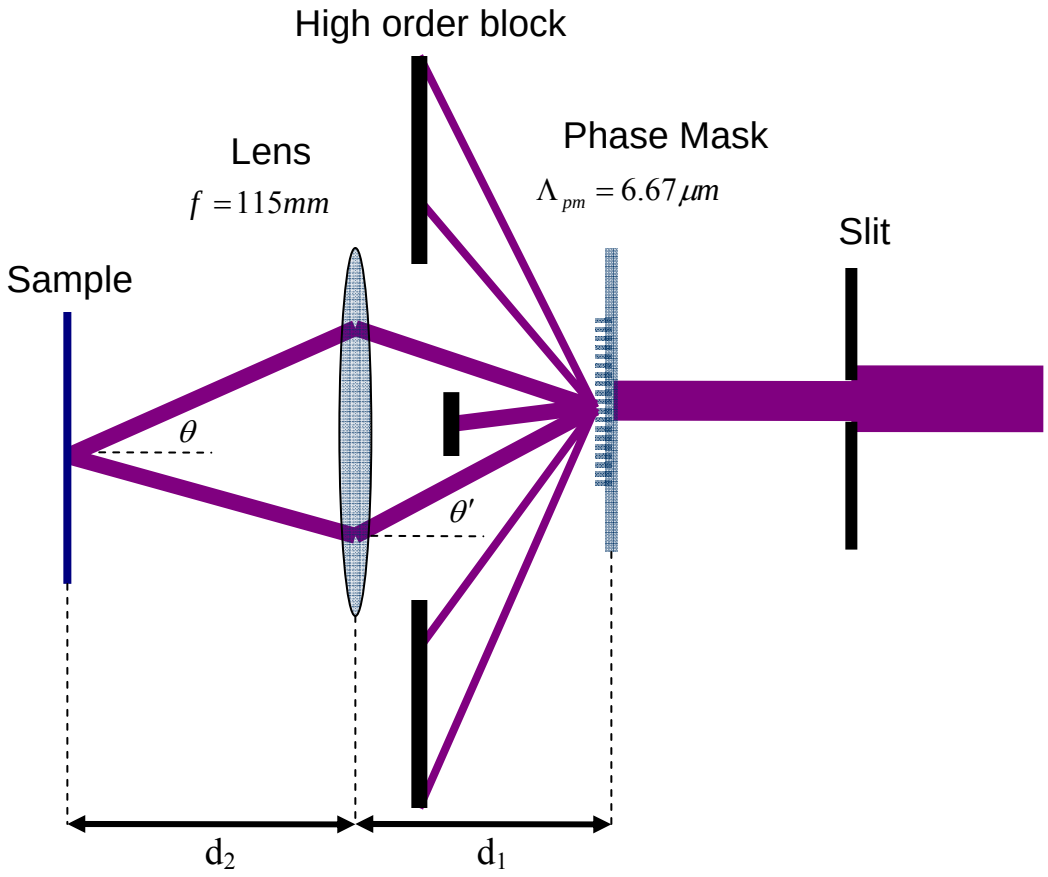

Figure 12 Grating fabrication optical components

4.1.5 Parameters for grating fabrication period

In the Fraunhofer limit, the two interfering beams at the sample surface can be written as plane waves.

$$E_{+1} = E_0 e^{ik(\cos\theta z + \sin\theta x)} \quad , \qquad E_{-1} = E_0 e^{ik(\cos\theta z - \sin\theta x)} \quad . \tag{31}$$

The intensity of the interfering beams is then simply the magnitude squared of the sum of the individual waves.

$$
\begin{aligned}
I &= \left|E_{+1} + E_{-1}\right|^2 \\
&= \left|E_0\right|^2 \left|e^{ik\sin\theta x} + e^{-ik\sin\theta x}\right|^2 \\
&= 4\left|E_0\right|^2 \cos^2\left(k\sin\theta x\right) \\
&= 2\left|E_0\right|^2 \left[\cos\left(2k\sin\theta x\right) + 1\right] \ .
\end{aligned}
\tag{32}
$$

The interference pattern then has a characteristic period

$$
\Lambda_g = \frac{\lambda}{2\sin\theta} \ . \tag{33}
$$

Eq. (33) allows one to calculate the grating period Λ_g which will be created when the beams interfere at the sample. θ and hence Λ_g can be determined by calculating the transfer function of the system. The output of an optics system in the paraxial ray limit in general can be written as [17]:

$$
\begin{bmatrix} y \\ \theta \end{bmatrix} = \mathrm{T} \begin{bmatrix} y' \\ \theta' \end{bmatrix} \tag{34}
$$

Where T is a 2x2 matrix representing the transfer function of the system. For the laser fabrication system, the transfer function can be written as [17]:

$$
\begin{aligned}
\mathrm{T} &= \begin{bmatrix} 1 & d_2 \\ 0 & 1 \end{bmatrix} \begin{bmatrix} 1 & 0 \\ -\frac{1}{f} & 1 \end{bmatrix} \begin{bmatrix} 1 & d_1 \\ 0 & 1 \end{bmatrix} \\
&= \begin{bmatrix} 1 - \frac{d_2}{f} & d_1 + d_2 - \frac{d_1 d_2}{f} \\ \frac{1}{-f} & 1 - \frac{d_1}{f} \end{bmatrix}
\end{aligned}
\tag{35}
$$

Here I have used the paraxial approximation as well as the thin lens approximation [17]. This transfer function accounts for the free space propagation after the phase mask, the lens and the subsequent propagation from the lens to the sample. It is assumed that the height of the ray at the start of the system and at the

output of the phase mask is zero, i.e. $y' = 0$, and similarly when the beams recombine at the sample $y = 0$. The angle at the output of the phase mask, θ', can be rewritten using the grating equation, Eq. (24) and similarly the angle at the output of the system, θ, can be written in terms of the desired grating period, Λ_g, using Eq. (33). Substituting these equations along with Eq. (35) into Eq. (34) and employing the paraxial approximation to simplify Eq. (24) and (33), we obtain

$$\begin{bmatrix} 0 \\ \frac{\lambda}{2\Lambda_g} \end{bmatrix} = \begin{bmatrix} 1-\frac{d_2}{f} & d_1 + d_2 - \frac{d_1 d_2}{f} \\ \frac{1}{-f} & 1-\frac{d_1}{f} \end{bmatrix} \begin{bmatrix} 0 \\ \frac{-\lambda}{\Lambda_{pm}} \end{bmatrix} . \tag{36}$$

Eq. (36) can be used in a number of ways. However, for fixed values of λ, Λ_{pm} and f it can be used to solve for d_1 and d_2 in terms of Λ_g. Solving (36) for d_1 and d_2 we have:

$$d_1 = \left(\frac{\Lambda_{pm}}{2\Lambda_g} + 1 \right) f \quad , \tag{37}$$

$$\begin{aligned} d_2 &= \left(\frac{2\Lambda_g}{\Lambda_{pm}} + 1 \right) f \\ &= \frac{2\Lambda_g}{\Lambda_{pm}} d_1 \qquad . \end{aligned} \tag{38}$$

Using Eq. (37) and (38), the appropriate distances can be determined for the fabrication of any desired grating period, Λ_g.

4.2 Grating fabrication alignment and characterization

4.2.1 Focus and alignment

Although the approximate relative locations of the phase mask, lens and sample can be calculated from Eq. (39) and (40) for a desired grating period, limitations in measurement and space on an optics table inhibits accuracy when setting up and aligning the system. In order to actually fabricate a grating, an iterative process of moving the lens, which is located on the Z stage, is carried out to find the optimal position of the lens.

The software is designed such that one can specify a start and end point along the X axis to do a scan. The scan works by moving the sample in steps specified by a step size. In addition a start point and step size is selected for the Z stage. At each movement between steps, the sample is moved by a fixed amount along X while the lens is moved by a fixed amount along Z. At each step the laser is fired. The focus determination process is carried out anytime any of the optical components are changed.

A typical alignment procedure would start with a 3 inch Si wafer with a layer of BCB. The sample is mounted on the stage. The stage is moved to expose the far left side of the sample to the beam path. The software is then setup to scan from left to right varying the position of the lens with each step. The number of laser shots at each interval is also specified. The stage is centered such that the center of the Si sample is approximately at the center of the stage coordinates. Typical parameters for alignment are shown in table 2. All position and step quantities are in μm.

X start	-30,000
X stop	30,000
X step	1,000
Z Start	10,000
Z step	-1000
Laser Shots	2

Table 2 Typical focusing determination parameters

After completion of a scan, depending on whether or not gratings have actually been fabricated, i.e. a good focus has been determined, the Z parameters will be adjusted. If another scan is desirable the sample is moved vertically to a different Y location and a similar scan will be performed again. Initial characterization of grating quality for this process is carried out through a rough visual inspection to look for gratings or other signs of ablation. The Z parameters are continually varied until visual inspection reveals gratings.

4.2.2 Characterization

If visual inspection is acceptable, the gratings are then viewed under an optical microscope to determine the optimal focus position/step of the Z axis. In addition, the grating period is characterized. An example of a grating coming into focus due to variation of the Z axis is show in Fig. (13). The images were taken at a magnification of 100X. Moving from left to right in the figure, the distance between the lens and sample is increased. As a result the location where the beams interfere on the sample changes. Once the two beams begin to overlap a region with gratings is formed. In Fig. (13), moving from left to right, in the first frame the two beams are not overlapping and no gratings are produced. Gratings first start to appear in the

second frame and maximize in the third. The gratings can be identified by the dark regions were the two beams are overlapping. By the fourth frame, the beams are starting to move past each other and consequently only a small area with gratings is present. Although it is not obvious at this magnification whether gratings actually have been formed, the dark region suggests the absence of light, which would be characteristic of a region with gratings because the gratings would act to diffract light away from the microscope.

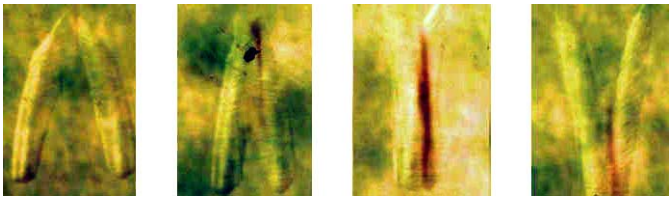

Figure 13 Focusing of laser via adjustment of Z axis to optimize grating fabrication.

Fig. (14) shows a 1000X image of the gratings. The grating period and total width of the grating area have been measured. These gratings roughly have a useable area on the order of $69.1\mu m$. A region consisting of 10 periods of the gratings is marked at $8.8\mu m$, suggesting that the period of the gratings is $\sim .88\mu m$. Taking a closer look at Fig. (15), the gratings appear to be uniform and well defined.

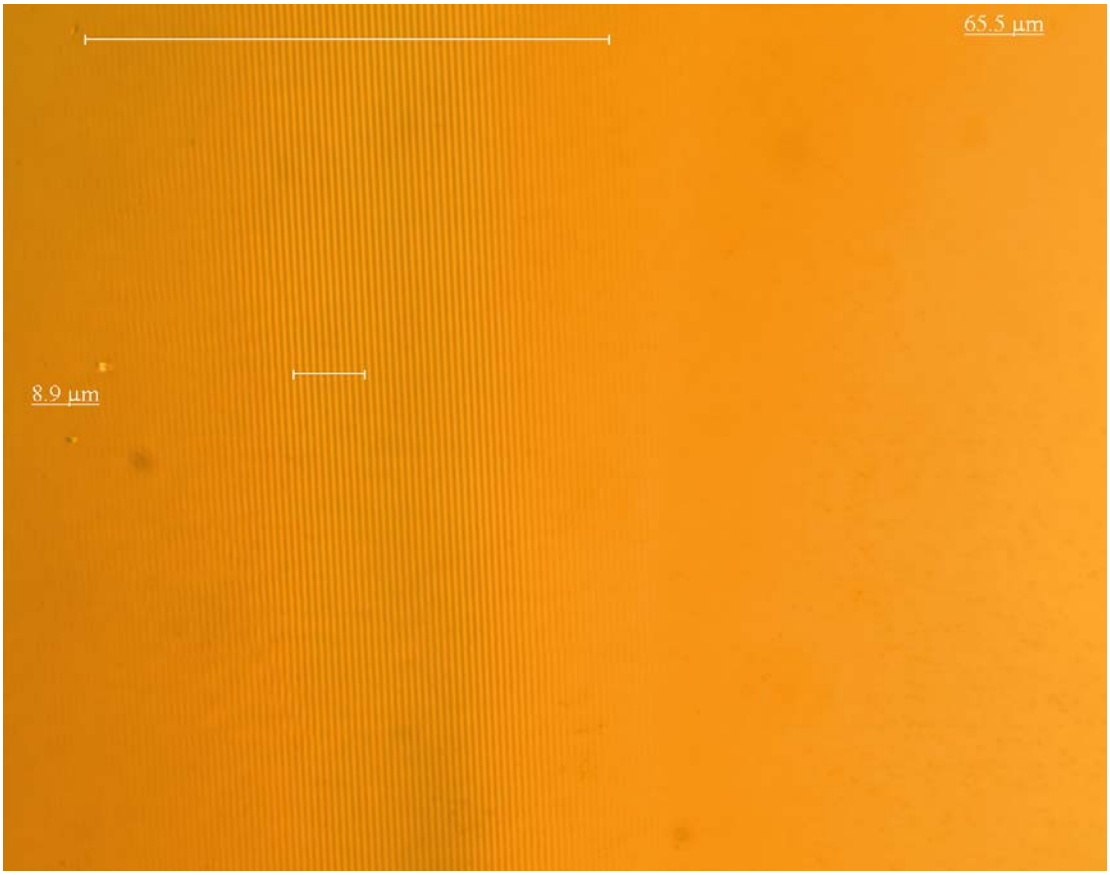

Figure 14 1000X image of gratings

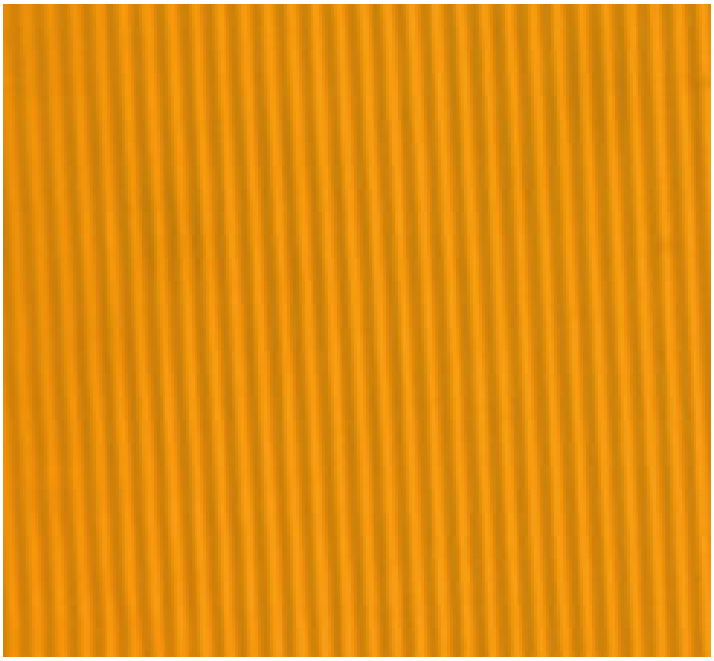

Figure 15 Zoom of Fig. (14)

For highly detailed images of the gratings, the sample is cleaved along the axis of the grating period and viewed using a scanning electron microscope (SEM). An SEM image of the grating cross section is shown in Fig. (16). The gratings are symmetrical and uniform. Upon closer inspection of the 50,000X image, debris is observed on the grating structure. For BCB and PI, debris left over due to the ablation process was typical. However, a cycle in an oxygen/plasma cleaner effectively removed the debris leaving a clean structure.

SEM images also allowed for the characterization of the grating height. Grating height could vary significantly as it is primarily a function of the amount of applied laser power. The output from the laser generally changes on a daily to weekly basis as it is a strong function of the amount of gas in the laser system, which slowly leaks with time. The leakage leads to a decrease in output laser power. Following a refill, the laser then returns to a higher level of output power. This scenario in general did not allow for accurate characterization of the grating height as a function of power. For transmission and coupling experiments, gratings were fabricated with various levels of power (by changing the number of laser pulses), and if desired, the grating heights could later be determined by inspection of an SEM image of the cross-section.

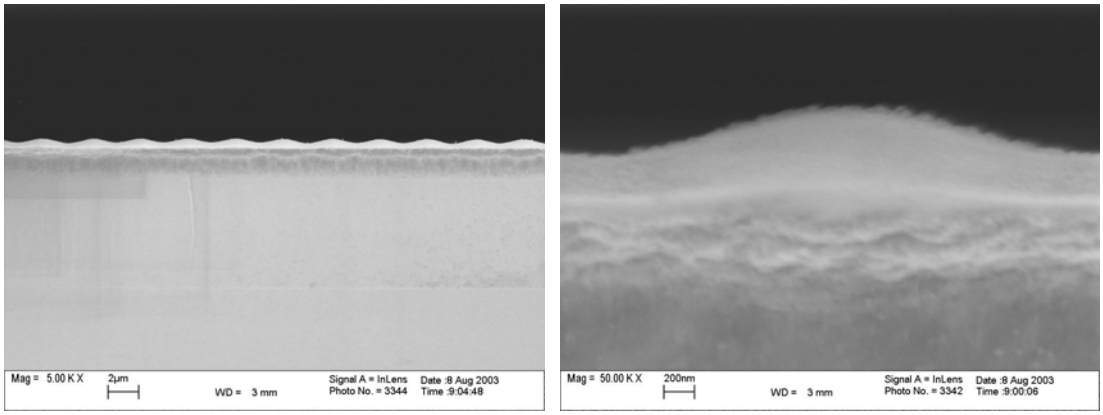

i. ii.

Figure 16 5,000X (i) and 50,000X (ii) SEM cross-section of gratings

4.2.3 ArF laser spectrum and limitations on grating width

As gratings were fabricated it started to become clear that there existed a fundamental limitation on the maximum width (along the grating period) of the gratings. Despite the size of the width of the slit being imaged on the sample, the width of the area where modulation or gratings were formed seemed to be limited. However, the vertical height of the gratings did not suffer from the same limitation. The spectral purity of the ArF laser was investigated as a possible cause.

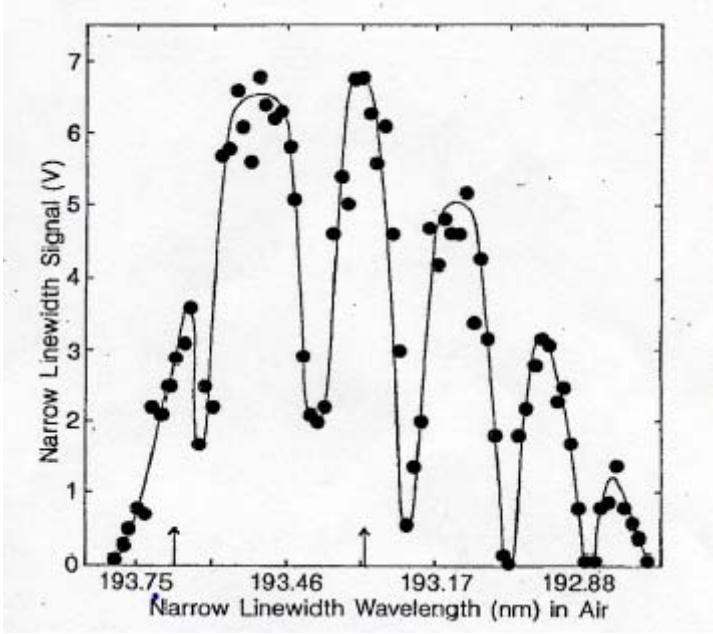

Figure 17 Spectrum of typical ArF laser output in air [20].

As seen in Fig. (17), the ArF spectrum consists of a number of well defined peaks. Because we are using transmission optics to focus the ArF laser, individual modes of the laser will each refract through the focusing lens at slightly different angles due to the various effective focal lengths for each respective wavelength. Eq. (38) can be rearranged to highlight the dependence of the output grating period on the focal length of the lens,

$$\Lambda_g = \frac{\Lambda_{pm}}{2}\left(\frac{d_2}{f} - 1\right) . \tag{41}$$

Since each mode then gives rise to gratings with slightly different periods, the interference of these different grating periods will give rise to various interference or beating effects. This effect was investigated through a Matlab simulation of the grating fabrication system, now taking into account four wavelength peaks at 193.15, 193.35, 193.55 and 193.75 nm. The wavelength values are taken from Fig. (17). The

source code for this simulation can be found in Appendix 1.1. Fig. (18) shows the results of the Matlab simulation for interference of 1, 2 ,3 and 4 modes. The dark regions are areas where gratings will be produced. Fig. (18i) is for the case of a single mode. In this scenario there will be modulation across the entire region of the image. In Fig. (18ii), two modes are interfered together and beating peaks appear. However, each beat has similar intensity peaks leading to small regions of poor grating creation but overall a large area grating. In Fig. (18iii). it is seen that the three interfering modes give rise to a decrease in the left and right lobes, while in (18iv) the side lobes are further reduced leaving only a small region where strong modulation will exist.

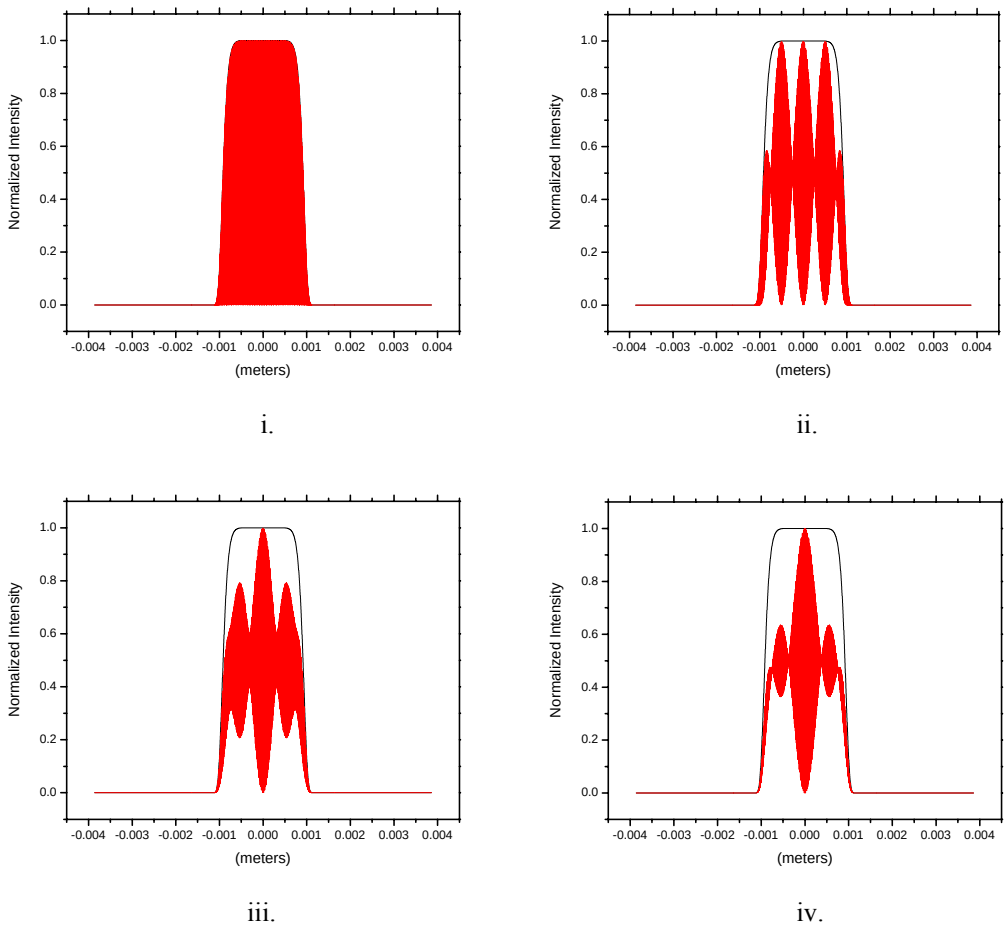

Figure 18 Interference patterns for various number of laser modes

The simulations in Fig. (18) were done in the ray optics limit assuming the paraxial approximation and a thin lens [14]. While these approximations are sufficient to show the beating effect, a much more accurate simulation was run in the wave approximation using Fourier optic methods [15]. The source code for this simulation can be found in Appendix 1.2. The results of this simulation are shown in Fig. (19).

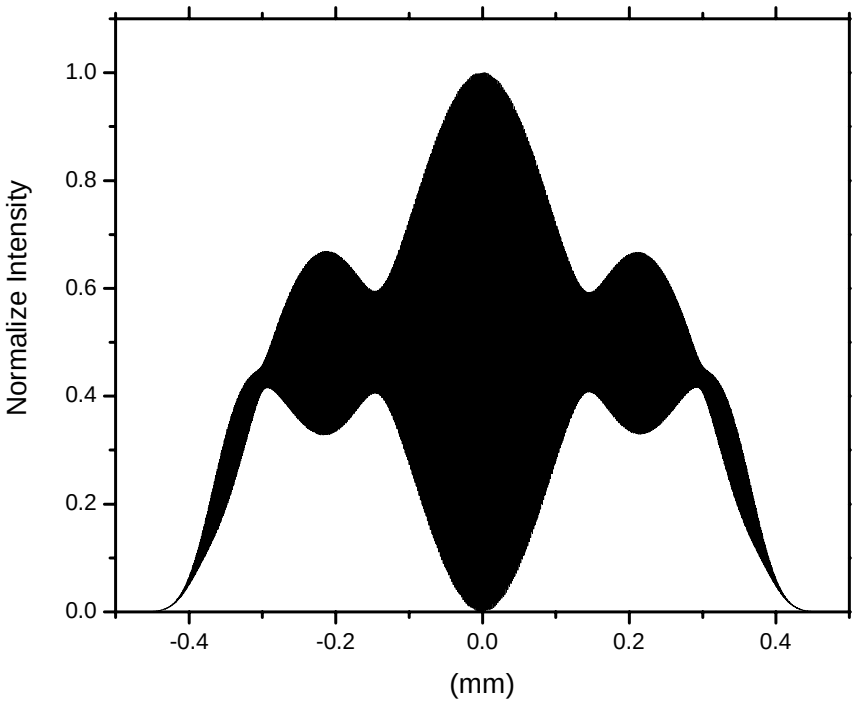

Figure 19 Accurate simulation of grating interference pattern.

The simulation was carried out for a fabricated grating period of 1 μm. The simulation has a 3 dB width of ~ 200 μm. However, modulation intensities within 30% of the peak will yield more usable gratings limiting the width to ~150 μm. This value is in agreement with our experimentally fabricated gratings.

4.3 Blazed gratings

With a symmetric grating, power distribution into each order is symmetric with respect to the fundamental order. As was discussed in section 2.6, when using diffraction gratings as couplers only a single diffracted order can be coupled into a single guided mode. Therefore it is ideal to have as much power as possible diffracting into a single order. As will be discussed in section 5.1, the power distribution into the diffracted orders can be altered by changing the grating shape, i.e., moving from a symmetrical to an asymmetrical grating profile will lead to an asymmetrical distribution of power into the diffracted orders. The process of creating an asymmetrical grating shape is commonly referred to as blazing [16]. It was decided that the best way to adjust the grating profile created by the interference of the two beams would be accomplished by tilting the sample. An attachment was designed which was connected to the main XY stage to allow the tilting of the sample at various angles. For our convention, the label the angle that the sample is tilted at as the blaze angle. The modified stage is depicted in Fig. (20). Various gratings were made at different blaze angles of 10^o, 20^o, 30^o and 40^o. SEM cross-sections of 10^o and 20^o blazed gratings are shown in Fig. (21), and an image of a 30^o blazed grating is shown in Fig. (22). As seen in the figures, as the blaze angle increases the shape becomes more asymmetrical and more specifically, begins to take on a triangular shape. An experimental study of the redistribution of power due to the blazed shapes is discussed in chapter 5.

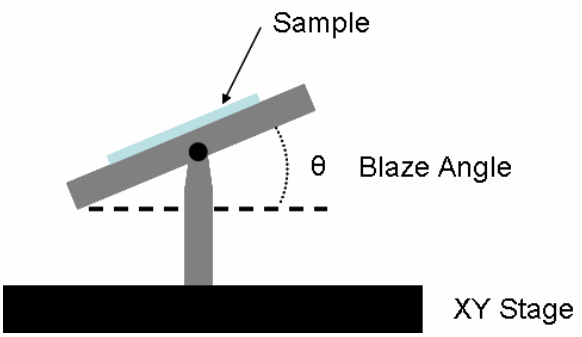

Figure 20 Modified stage used for tilting sample to blaze grating profile.

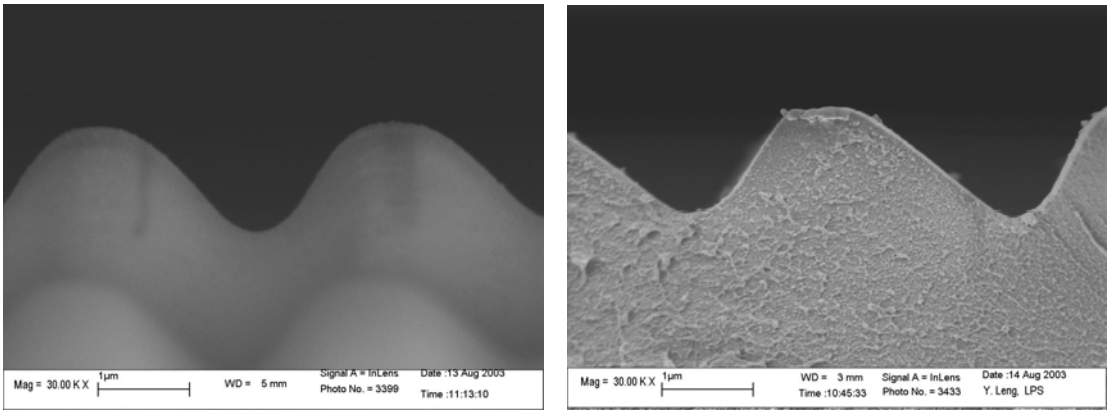

i. ii.

Figure 21 30kX SEM image of 10^o (i) and 20^o (ii) blazed gratings

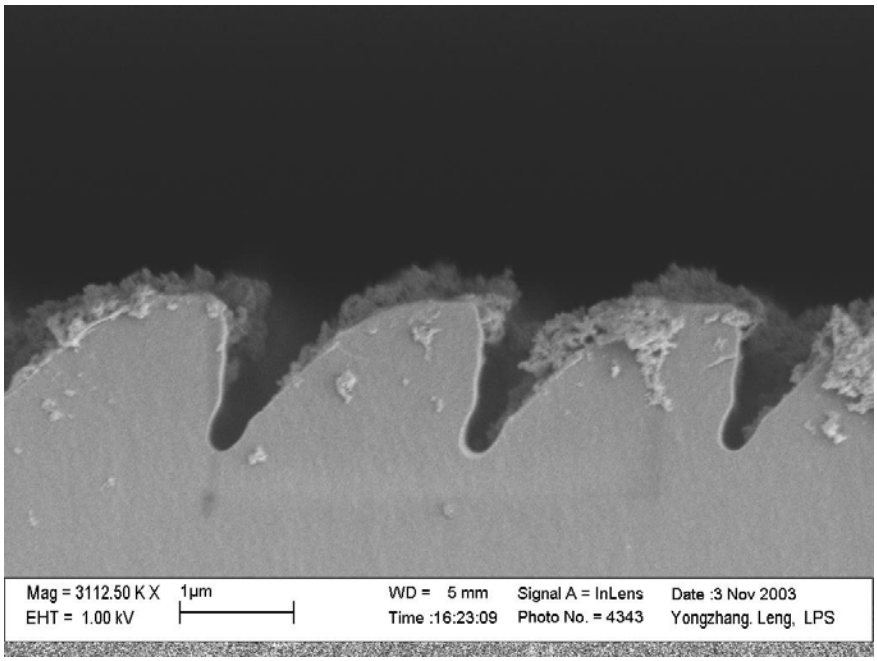

Figure 22 50kX SEM image of 30^o blazed grating

Chapter 5: Measurement and Characterization

5.1 Transmission measurement and theoretical calculation

5.1.1 Experimental objectives and setup

In order to determine the power distribution of our gratings for both the symmetric and asymmetric case, transmission measurements were carried out. We were interested in determining how diffracted power shifted into various orders as we changed both the depth of the grating by varying the power and number of excimer laser shots and the blaze angle of our sample. The primary goal was to shift the power out of the fundamental into a single first or second order beam so that this beam could be efficiently coupled into a waveguide.

A sample was prepared that consisted of a glass slide that had a 5-6 μm layer of BCB. Gratings were then fabricated on the film using the laser fabrication system. Symmetric gratings were fabricated for a reference, and blazed gratings were produced at various blaze angles in increments of 10^o. The grating period was chosen arbitrarily to be 2.2 μm. For testing, the sample was illuminated at normal incidence with a HeNe laser. A power detector with wide detection area was then used to measure the power of each diffracted beam. The experimental setup is illustrated in Fig. (23).

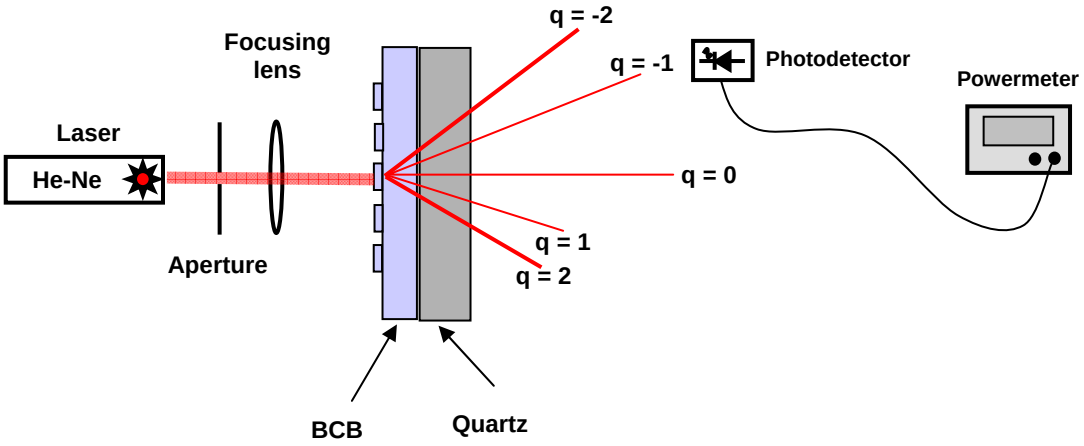

Figure 23 Transmission Measurement

5.1.2 Results

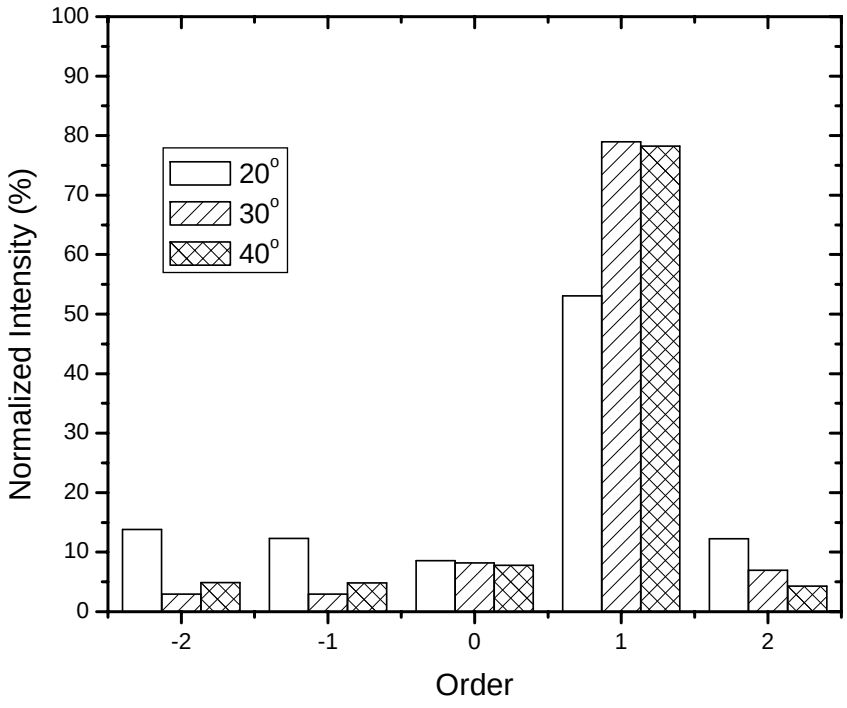

Figure 24 Power Distributions for Various Blaze Angles

Fig. (24) shows the distribution of power that we measured for blaze angles of 10, 20 and 30 degrees. In all cases there was a significant amount of power shifted into the first order, which was our primary goal. From our data, any sample produced with a blaze angle around 30^o exhibited very good results. Fig. (24) shows a comparison between a symmetric grating and a blazed grating (30^o). The symmetric grating, as expected, has equal power distribution around the zeroth order. In addition, the power in each order decreases as one goes to higher orders, which is similar for the case of a periodic array of slits. The blazed grating, on the other hand, is highly asymmetric with almost 80% of the power going into the first diffracted order. This shift is highly desirable.

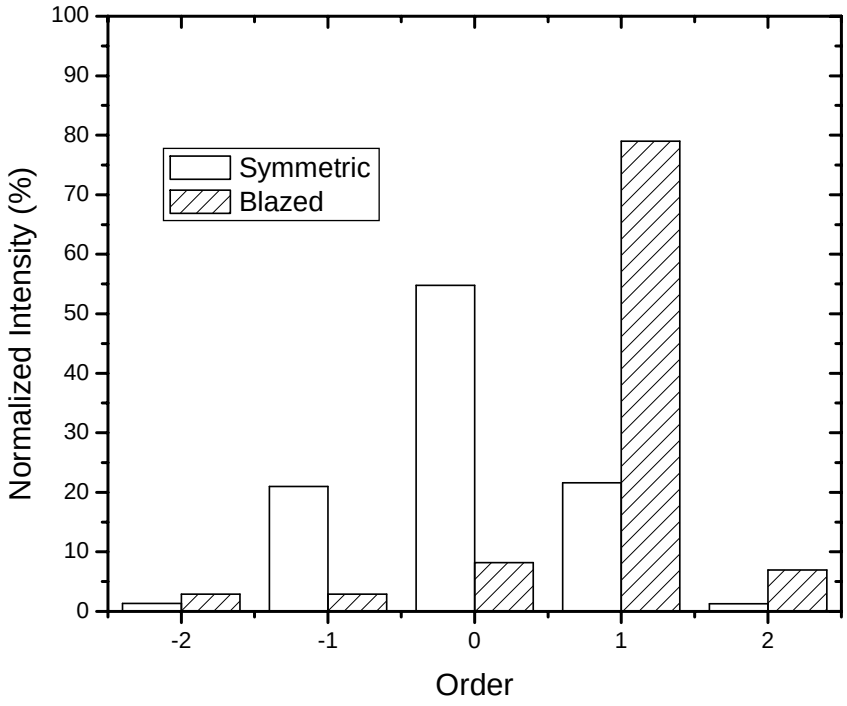

Figure 25 Symmetric grating vs. blazed grating

5.1.3 Theoretical calculation

A theoretical calculation can be performed to calculate the power distribution due to the diffraction of various shaped gratings. As was mentioned in section 2.4, the diffraction due to one element of the grating is proportional to the Fourier transform of the transfer function of the element. For phase gratings illuminated at normal incidence, the transfer function is just a phase change that the incident light undergoes due to the differences between the index of refraction of air and the polymer.

$$t(x) = e^{ik_0(n-n')g(x)} \quad . \tag{42}$$

Where n' and n are the indexes of refraction for the source medium and grating medium, respectively, and g(x) is a function describing the shape of the grating. In general, analytical solutions to the Fourier transform of a transfer function such as Eq. (42) are not possible. However, numerical solutions are trivial to calculate with math programming packages such as Matlab, Mathcad or Mathematica. Theoretical calculations for this project were carried out using Matlab. The associated code can be found in Appendix 1.3.

Eq. (43), (44) and (45) give the transfer function for a single diffraction element of a sinusoidal phase grating, saw tooth phase grating and slit amplitude grating, respectively, and $u(x)$ is defined as the unit step function. Fig. (26) shows a comparison between the Fourier transforms of these three transfer functions for the same grating period $(2.3\mu m)$, grating depth $(0.4\mu m)$ and wavelength $(.632\mu m)$. The slit amplitude grating does not have a depth but rather a characteristic width for which

I choose to be 15% of the grating period for this simulation. The Fourier transforms were evaluated numerically using the code in Appendix I.

$$t(x) = e^{ik_0(n-n')\frac{g_{depth}}{2}(\cos(2\pi\frac{x}{d})+1)}\left[u(x)-u(x-d)\right] , \tag{43}$$

$$t(x) = e^{ik_0(n-n')g_{depth}\frac{x}{d}}\left[u(x)-u(x-d)\right] , \tag{44}$$

$$t(x) = \left[u(x+\frac{a}{2})-u(x-\frac{a}{2})\right] . \tag{45}$$

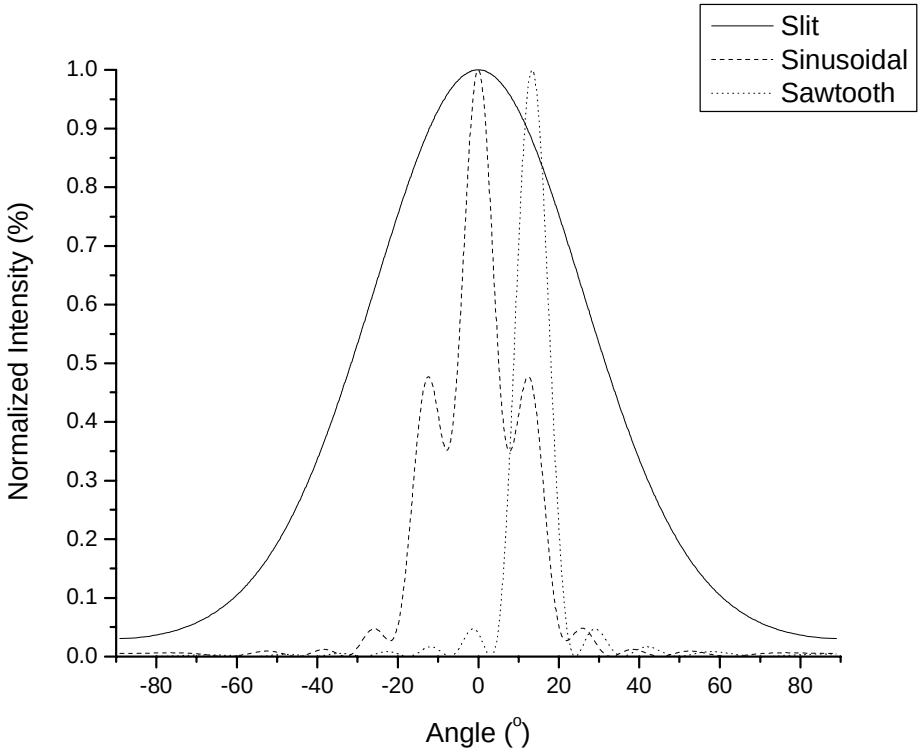

Figure 26 Theoretical calculation of the normalized intensities of the far field diffraction pattern for various diffractive elements.

The slit and sinusoidal diffraction patterns both have symmetric diffraction patterns, as expected. Comparing the slit and sinusoids, it appears that a sinusoidal

grating will confine more of the energy into lower order beams. However, the same can be true for a slit as the width of the slit is increased. For this simulation, as was previously mentioned, the slit had an opening equal to 15% of the grating period. But if this opening was increased to 50%, a diffraction pattern very similar to the sinusoidal pattern would be observed, and consequently much more of the power would be confined to the lower orders. The main problem with the amplitude grating does not lie in its diffraction pattern however, but in is efficiency to transfer the input power to the output. With a phase grating, while there will be a reflection at the interface, which is predicted at any boundary between two materials of different indices, if the index difference is small then the total reflection can easily be less than 10% for interfaces such as air and glass. However, with the amplitude grating, all of the light incident on the blocking portion of the diffraction element will be lost. So in my simulation for the amplitude grating only 15% of the incident power would actually be transmitted. In addition the physics behind the absorption and reflection at this blocking surface need to be considered. Specifically, if the input intensity is too high, it is very easy to damage an amplitude grating due to the heat buildup that can occur due to the absorption at the blocking part of the grating. By working with phase gratings which are generally made of transparent materials (for the wavelength of the particular application), both the efficiency and damage issues can be circumvented.

5.1.4 Comparison of measured and theoretical data

Fig. (27) shows a comparison between the measured and theoretical power distribution for a symmetric grating. Both sets of data are in very good agreement.

The grating shape used for the simulation was obtained from an SEM cross section of a similar grating which was fabricated on a BCB layer on a Si substrate. The sinusoidal shape, height and period were all extracted from a SEM picture and used in the simulation [2].

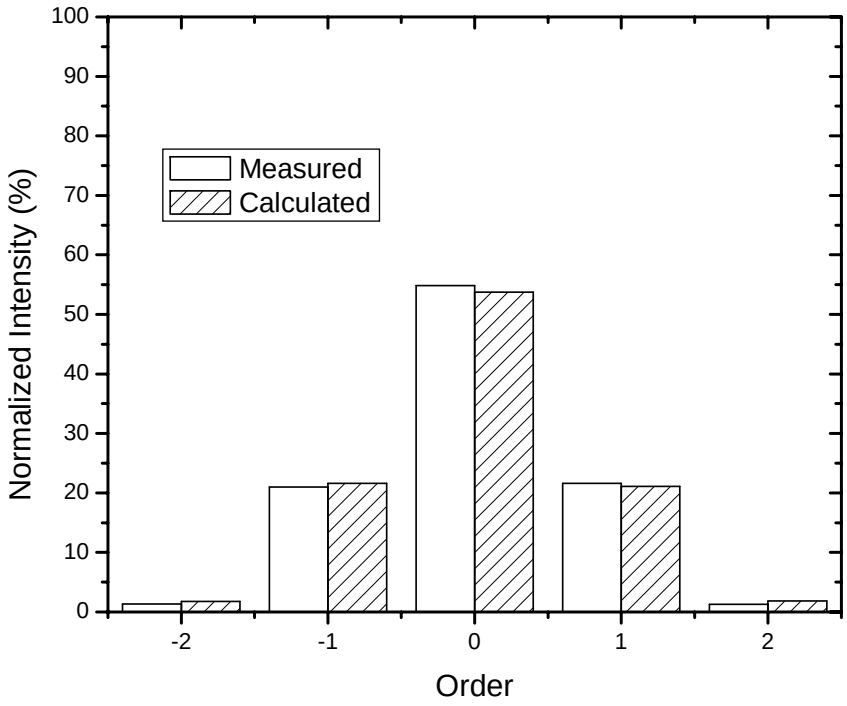

Figure 27 Measured vs. calculated power distribution for a symmetric grating

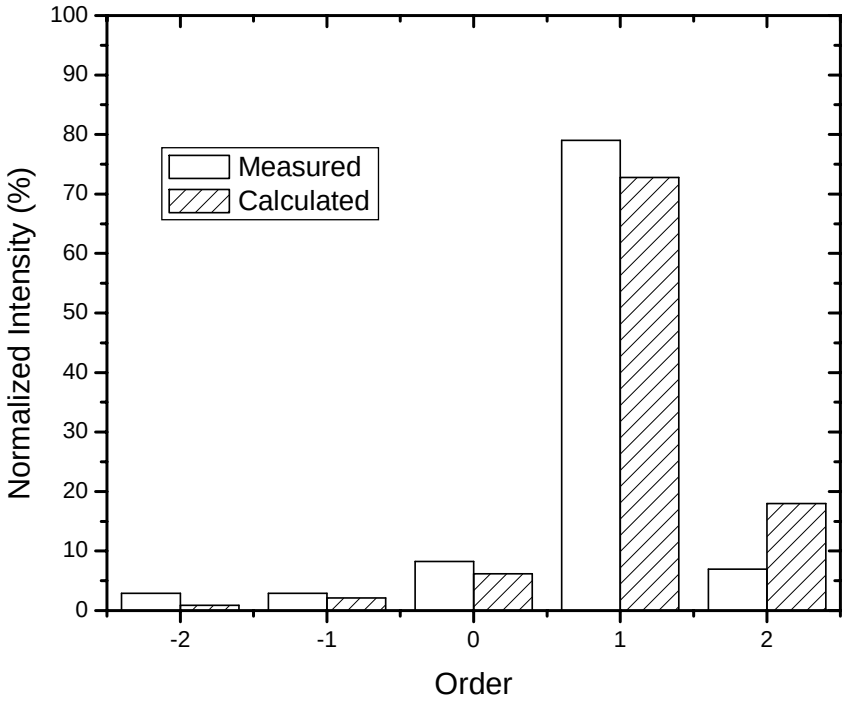

Figure 28 Measured vs. calculated power distribution for a blazed grating

Fig. (28) shows a measured vs. theoretical power distribution for a blazed grating fabricated at a blaze angle of 30^o. Once again, the theoretical results are in good agreement with the measured results. The grating shape, height and period were all extracted from an SEM photo of a similar grating fabricated on a Si wafer. Fig. (29) and (30) illustrate the grating and grating shape used in the calculation.

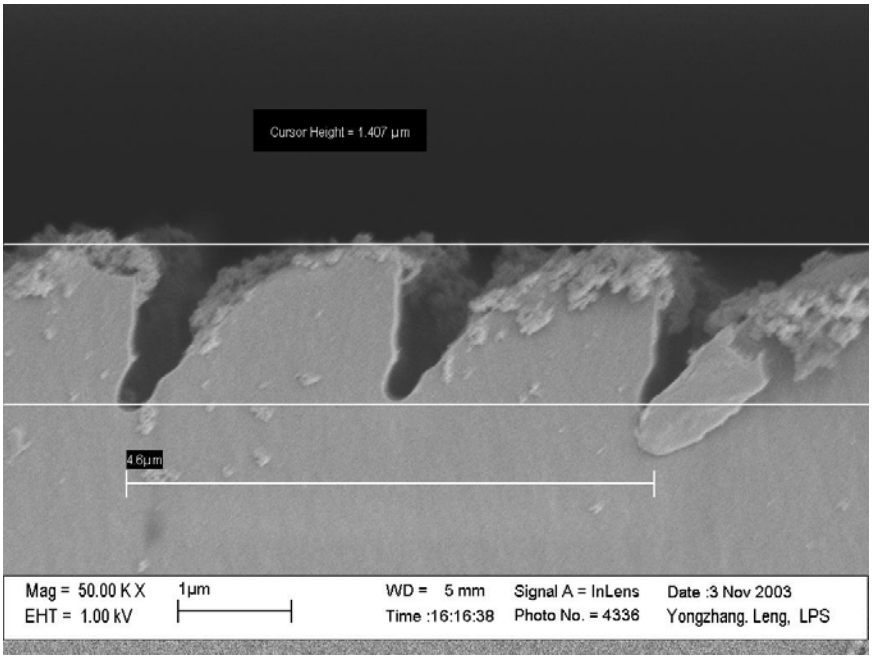

Figure 29 SEM photo of grating used to determine simulation parameters

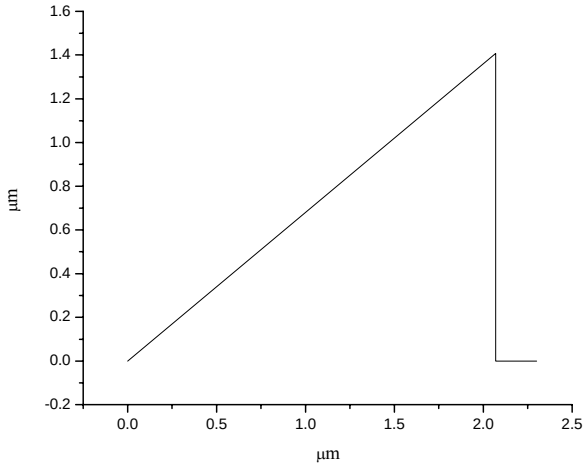

Figure 30 Simulated grating shape

5.2 Input coupling into dispensed multi-mode waveguides

5.2.1 The dispensed waveguide

In addition to spin coating thin films on surfaces the polymer optics group has also been working on directly dispensing polymer lines onto various surfaces [21]. These polymer lines are drawn with a polymer filled syringe which is moved with high precision stepper motors. The polymer is generally of the UV curing type and immediately after the line is drawn a UV light source is applied to cure the polymer. If the material below the polymer line is of lower index than the dispensed polymer then the polymer line can guide light. The waveguides typically have dimensions on the order of $\sim 9\mu m$ in height and $\sim 200\mu m$ in width and utilize a layer of SiO_2 as a cladding, which is grown on the Si substrate prior to the application of the polymer. A diagram of the dispensed waveguide along with its profile is illustrated in Fig. (31).

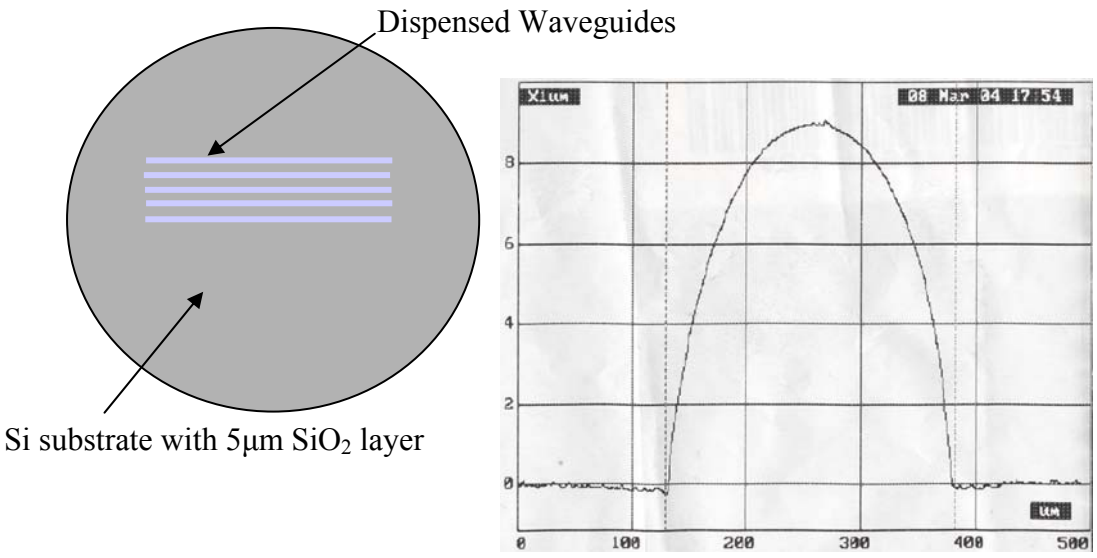

Figure 31 Schematic of polymer line drawn on Si substrate and profile of the line.

Gratings with a period of $1.7\mu m$ were fabricated on the waveguides. Fig. (32) shows an optical microscope picture of a dispensed guide with gratings on it.

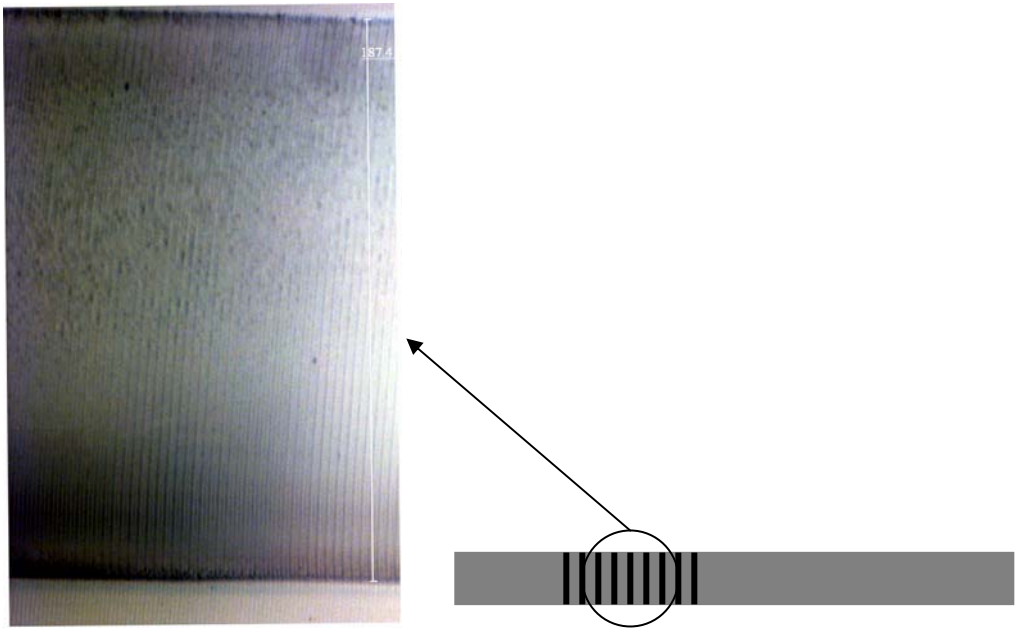

Figure 32 Optical photo of section of dispensed waveguide with gratings.

5.2.2 Acceptance angle for coupling

Since the waveguide has a width of $\approx 200\mu m$ which is $>> 632nm$, (wavelength of a HeNe laser) the waveguide was treated as a slab in the horizontal direction for calculation purposes [17]. The first 15 modes were calculated for the configuration show in Fig. (33).

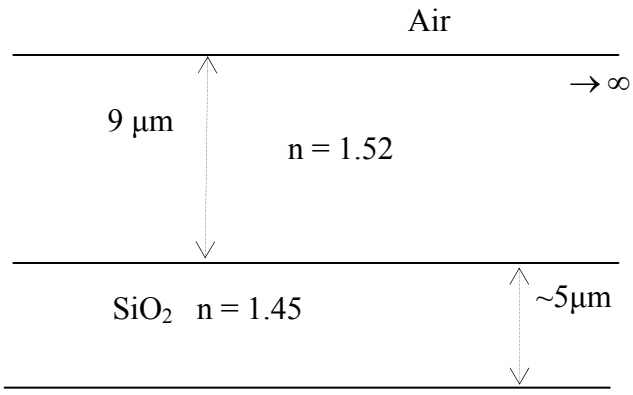

Figure 33 Schematic of waveguide used for mode calculation

Next, using Eq. (30) the acceptance angles were calculated for the various diffraction orders of the grating and modes of the waveguide. Fig. (34) is a graph of the results of this calculation. We see that there exists two bands of acceptance angles around 60^o and 15^o for the first and second orders respectively.

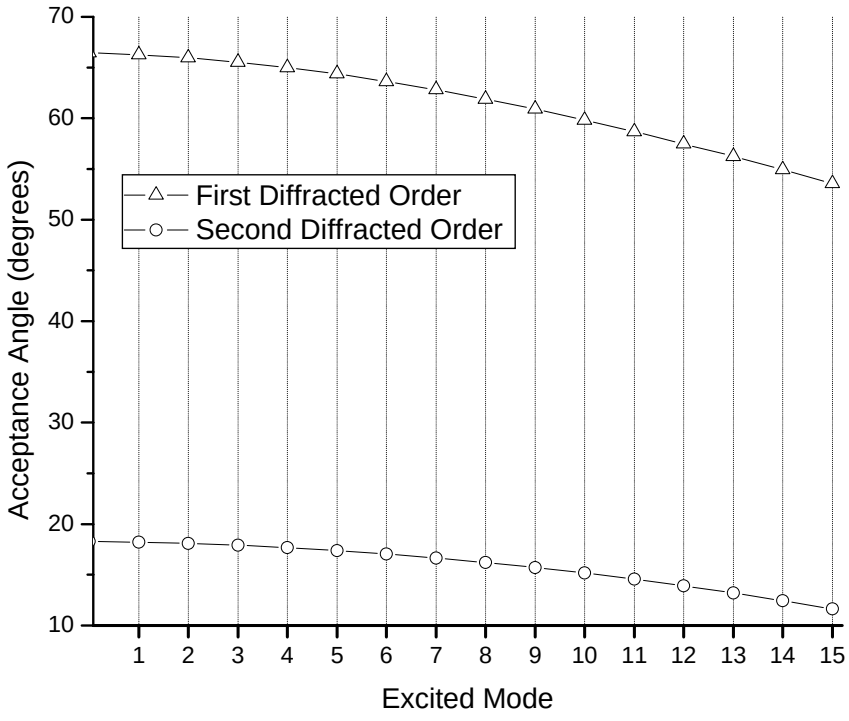

Figure 34 Graph of excited mode vs. acceptance angle

5.2.3 Demonstration of input coupling

An apparatus was designed and fabricated which would allow the sample to be rotated on an axis such that input coupling could be observed at various angles. The apparatus consisted of a vacuum chuck mounted to a three way stage which was mounted on a rotating stage. The sample was then illuminated with a HeNe source. The light was focused onto the grating and the sample was rotated until input coupling was observed. A schematic of the apparatus and the experiment is illustrated in Fig. (35).

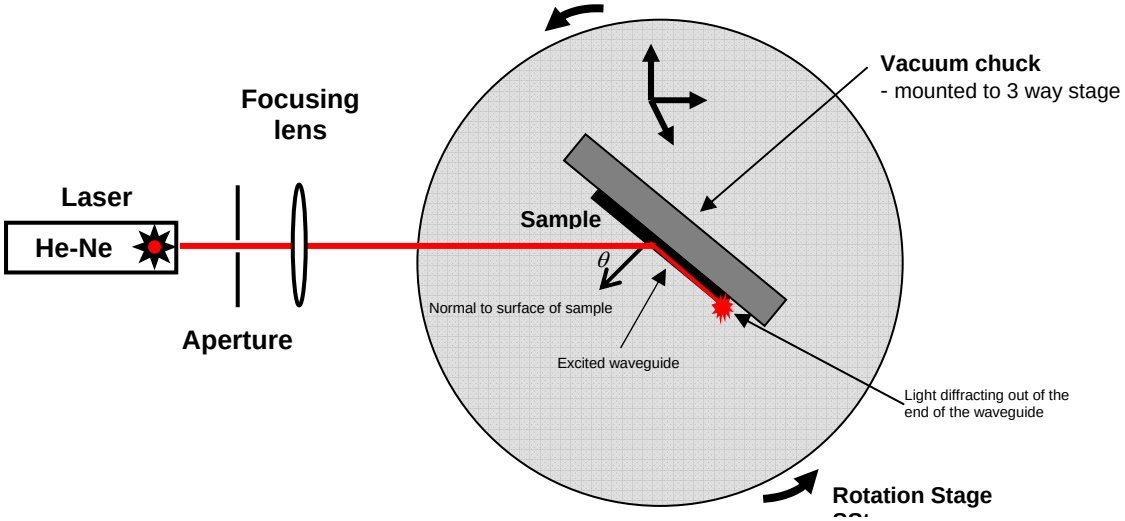

Figure 35 Schematic of input coupling experiment

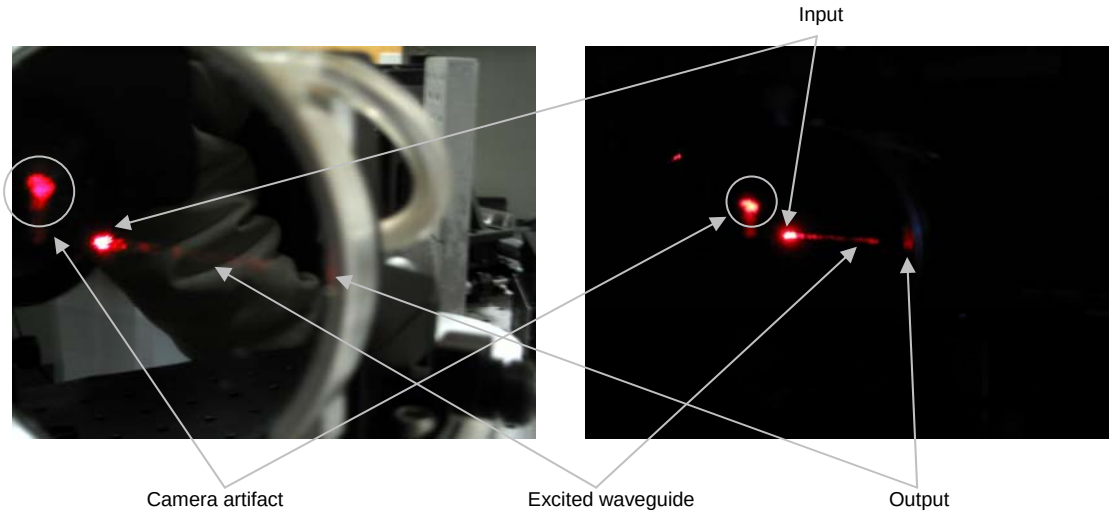

Figure 36 Photograph of excited waveguide

Fig. (36) consists of two photographs taken of the excited waveguide. The first is with the room lights on, the second is with the room lights off. Coupling was observed in two bands of angles around 15^o and 60^o which was in agreement with the theoretical calculation.

5.3 Output coupling from single-mode waveguides

5.3.1 Introduction

In addition to polymer dispensed waveguides, the LPS polymer optics group has also been designing and fabricating single and multimode waveguide using conventional lithographic techniques. For this experiment, single mode waveguides at 1550nm were designed and then fabricated. Gratings were fabricated on the waveguide and then, with the aid of a Newport automatic aligner, the output coupling efficiency was experimentally determined. In addition a theoretical calculation was performed as a comparison.

5.3.2 Design and fabrication of single mode waveguides

BCB and SiO_2 were chosen as the waveguides core and lower cladding materials respectively, with the upper cladding and side claddings consisting of air. Various three dimensional pedestal waveguides were simulated using the commercially available software package, BeamPROP^{TM} from RSoft Inc. A lithographic mask was already available which allowed for the fabrication of waveguides of widths 2.0 – 3.8 μm in steps of 0.2 μm. Vertical modes then for various heights of waveguides were calculated using the BeamPROP software. For the known index parameters of 1, 1.536 and 1.482 for the upper cladding, core and lower cladding, respectively, it was calculated that a waveguide with a height of ~2.7 μm and a width of ~3 μm would support a single mode at 1550 nm with an $\sim n_{eff} = 1.509$. Fig. (37) shows a schematic of the simulated waveguide along with the BeamPROP theoretical calculation of the mode. The SiO_2 layer thickness is arbitrarily chosen to be 5 μm. However, it should be noted that there is a small amount of leakage of the mode into the SiO_2 cladding and that if the SiO_2 is not thick enough then the wave could couple into the substrate.

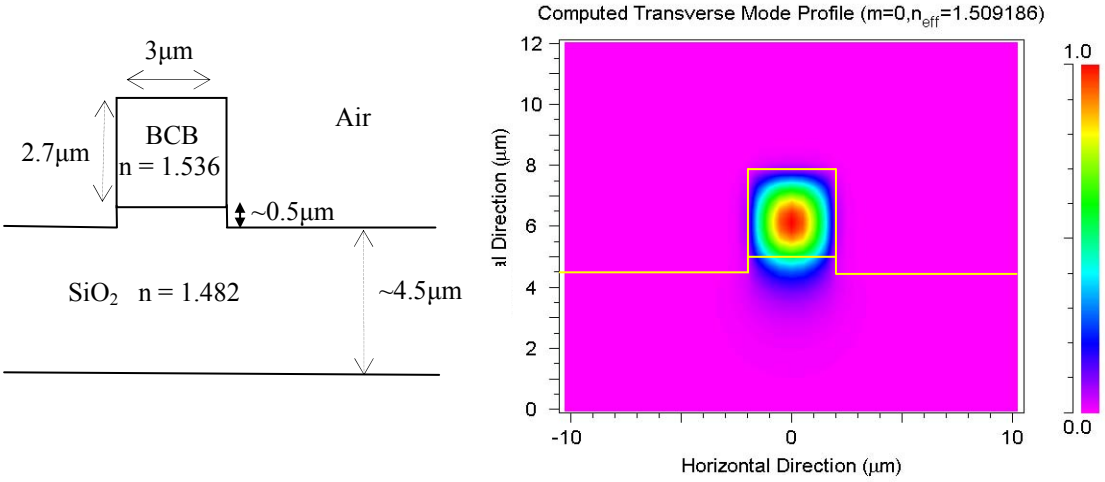

Figure 37 Schematic of single mode waveguide and computed mode profile

Fabrication was carried out using standard lithographic techniques. A 5 μm layer of SiO_2 was deposited on a silicon substrate via plasma enhanced chemical vapor deposition (PECVD). A 2.7 μm layer of BCB 3022-46 was then fabricated on the sample using the procedures outlined in section 2.2. The Waveguide was patterned using standard photolithography in which photo-resist was exposed with an i-line 5X projection aligner and developed. The photo-resist pattern was then transferred with reactive ion etching (RIE). In order to achieve pedestal waveguide structure, SF_6/O_2 and CHF_3/O_2 plasma was used to etch BCB and SiO_2, respectively. Fig. (38) shows a SEM photograph of the fabricated waveguides. The picture is from the top of the sample. Different width waveguides are distinguished from each other by markers which are patterned along with the waveguides. The marker gives the waveguide width in microns of the waveguides on either side of the marker.

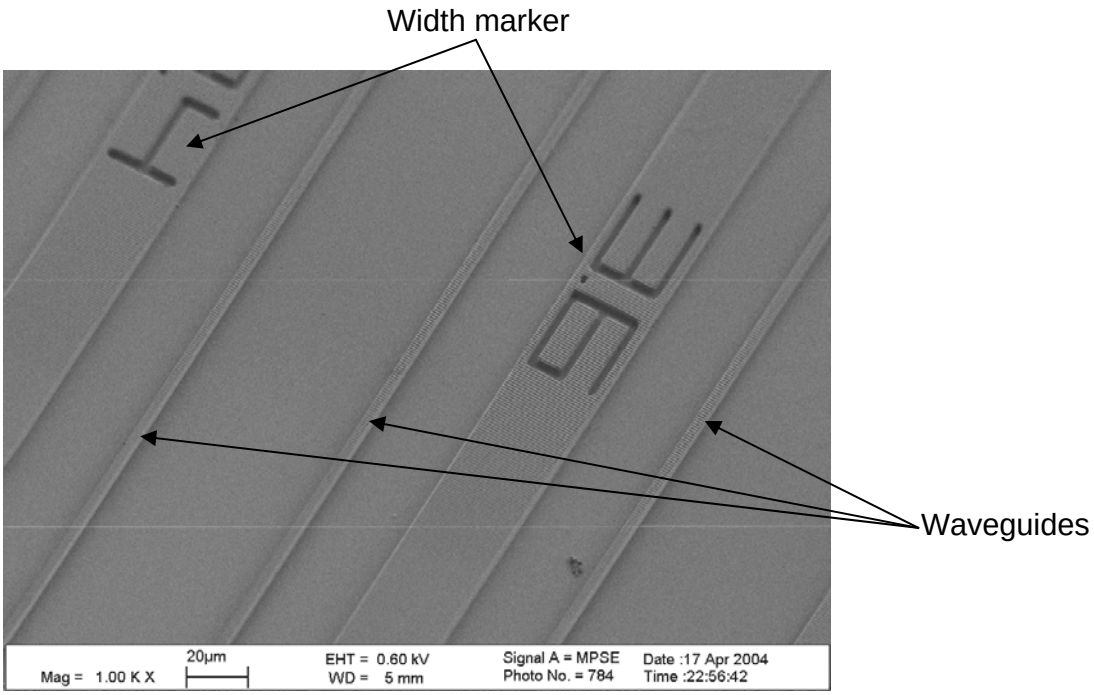

Figure 38 SEM photo (1000X) of lithographically fabricated BCB waveguides

5.3.3 Grating parameters and fabrication

For this measurement we are interested in determining how much output light we can capture from the grating. Since we wish to make the measurement as simple as possible, we designed the coupler such that there is only the +/-1 order leaving the grating. In addition having this order diffract vertically at 0^o with respect to the surface normal will also make the output simpler to measure, because a detector can be mounted directly above the grating coupler. In general though, vertical or 90^o coupling from integrated polymer waveguides could find uses in applications such as input coupling from VCSEL's and output coupling into vertical detectors [22]. We can rewrite Eq. (30) solving for the grating period,

$$d = \frac{m\lambda}{\left[n_{eff} - n'\sin(\theta')\right]} \quad , \tag{46}$$

where

$$n_{eff} = \frac{\beta}{k_o} = \frac{\lambda\beta}{2\pi} \quad . \tag{47}$$

Now knowing the order and the desired diffraction angle we can calculate the required grating period. For

$$\left.\begin{array}{l} m = 1 \\ n_{eff} = 1.509 \\ n' = 1 \\ \theta' = 0 \\ \lambda = 1550nm \end{array}\right\} \rightarrow d = 1.03\mu m \tag{48}$$

With the desired grating period in mind, gratings were fabricated on the single mode waveguides with the desired grating period. The sample was tilted at an angle of 30^0 during fabrication. Fig. (39) shows a 20,000 X SEM photograph of the waveguide with the gratings fabricated on it. The sample is tilted such that the top and side of the waveguide are visible.

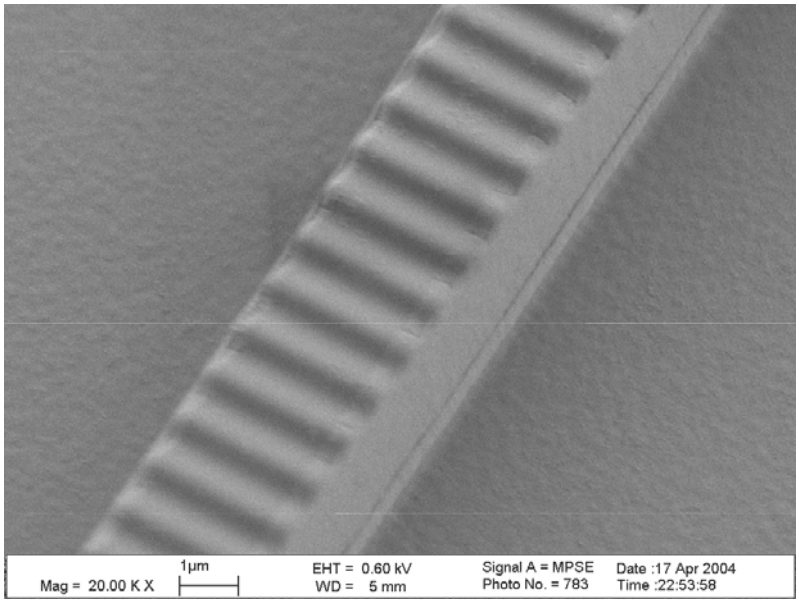

Figure 39 SEM photograph (20 kX) of polymer waveguide with gratings

5.3.4 Aligners

All measurements on the single mode waveguides were carried out using a computer controlled high precision aligner as in Fig. (40).

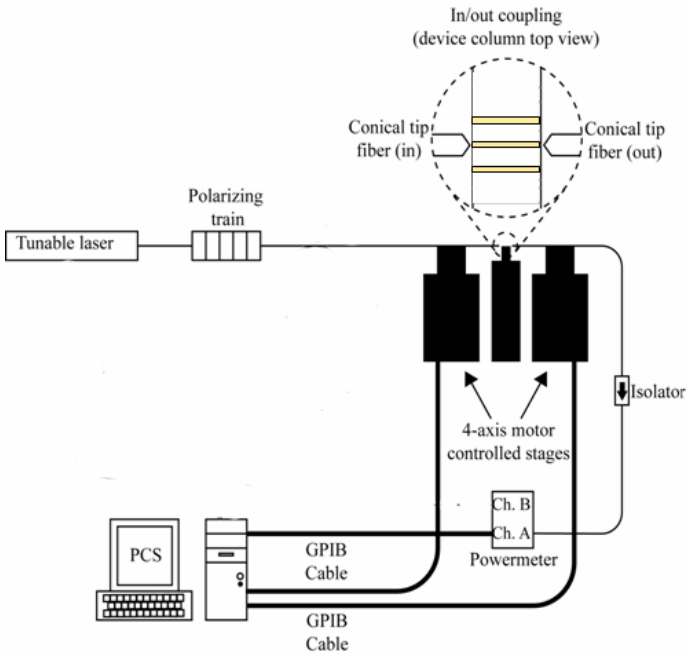

Figure 40 Diagram of standard computer controlled aligner

Aligners are used to align fibers to couple light efficiently into waveguide structures with dimensions on the order of microns. Aligners employ a lensed fiber which is used to focus light into the waveguide and another lensed fiber which is used to capture light coming out of the guide. The input and output fibers are generally connected to some sort of source and detector, respectively. The difficulty in this procedure lies in the efficient alignment of the input and output fibers with the waveguide. An aligner employs high precision stages to control the positioning of the fiber as well as the rotation of the fiber. The stages have resolutions on the order of 100 nm. A computer is connected to the stages and is also connected to a power meter which is monitoring the power in the output fiber. This provides a feedback

system which allows the computer to adjust the position of the input and output fibers until the optimal alignment is found. Once aligned, experiments can be performed on the waveguide.

One use for an aligner is for the determination of the characteristic loss of a waveguide [19]. A waveguide of known length is placed in the aligner and the total loss due to input coupling, propagation and output coupling is measured. The combination of all three loses is know as the insertion loss. The waveguide is then shortened and the insertion loss is measured again. Knowing the change in length and the change in the insertion loss one is able to determine the characteristic loss of the waveguide. The primary assumption here is that the change in the insertion loss is due only to the change in propagation length. In reality shortening the sample involves the cleaving of the sample which yields a new surface at the input or output which, can easily change the loss associated with the input and output coupling. The experiment can be repeated many times, however, to minimize this source of error.

5.3.5 Characterization of output coupling from waveguide

In order to perform a basic characterization of the gratings as output couplers, a waveguide with gratings was aligned and excited with a HeNe laser. The light output was then observed both visually and with a CCD camera. Fig. (41) shows a picture captured from a CCD camera of output coupling from the grating.

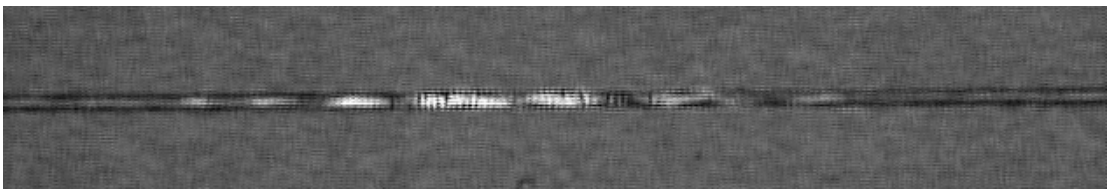

Figure 41 Light coupling out of grating

In addition, the waveguide was excited with a 1550 nm source. A detector was mounted above the grating area and a scan of the output light was performed. The scan was carried out using a detector with a diameter of ~3mm and at a scan height of ~17mm above the sample. A schematic for the setup and the measured output from the scan is shown in Fig. (42) and (43), respectively.

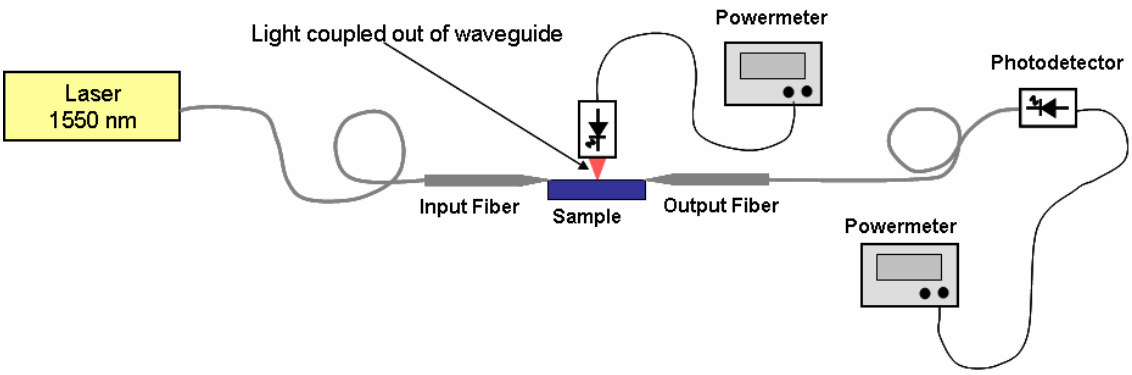

Figure 42 Schematic of power measurement for light coupled out of waveguide

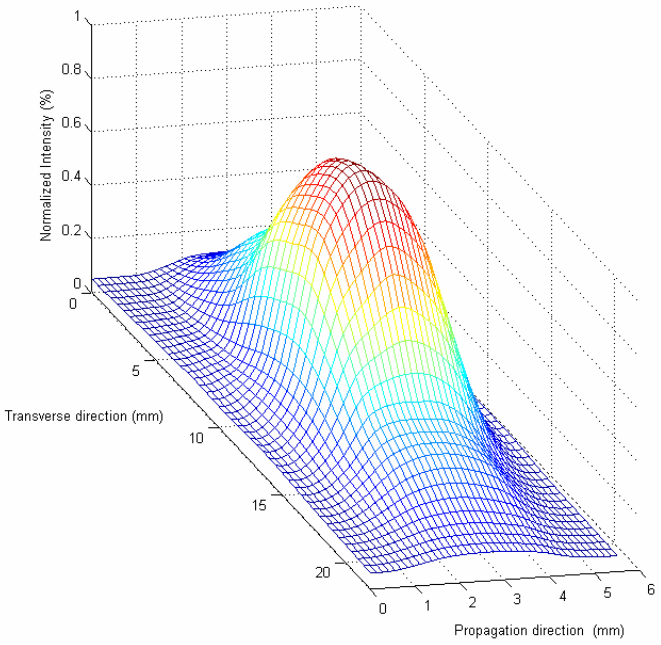

Figure 43 Scan of output from grating

Due to the size of the detector and the scan height used for the measurement, the scan does not represent the beam profile but rather the beam profile of the grating

convolved with the area of the detector. The scan is useful, however, in that it does suggest a uniform output from the grating. In addition it is obvious from the scan that the beam is diverging much faster in the transverse direction than in the propagation direction. This is to be expected as the length of the grating in the transverse direction is on the order of the width of the waveguide (~3 μm), while the length in the propagation direction is ~200 μm.

5.3.6 Output coupling efficiency measurement

In order to determine the coupling efficiency of the grating, the same power meter used to measure the output beam profile was placed above the sample as in Fig. (42). The waveguide was excited with a 1550 nm source and aligned. The detector position in space was adjusted to maximize the power reading. The detector ended up centered over the center of the grating and ~ 1 mm above the grating. The incoming polarization was then adjusted using the polarizing train located between the laser and the input fiber to maximize power. Detector positioning was rechecked and a power measurement was taken.

Prior to fabrication of gratings on the sample, the sample was excited and aligned and the detector was placed above the sample to get an idea of the amount of light which would be detected due to scattering from the waveguide. These numbers were then compared to the power output after fabrication of the grating, and in general, we took only 90% of the power meter reading to compensate for additional light that was scattered into the detector from sources other than the grating itself.

Typical insertion losses for the waveguides were measured and found to be on the order of 8-10 dB for 1 cm long waveguides. The gratings were fabricated in the

middle of the guide and therefore the total loss before the grating will be half of the insertion loss. As depicted in Fig. (44), for the coupling efficiency calculation a 4 dB loss due to coupling (3 dB) and propagation (1 dB) was assumed. Although this separation of the loss into a coupling and propagation component is unnecessary, a 1 dB loss for a 0.5 cm waveguide is in agreement with previous waveguide loss measurements and is depicted in the figure for clarification. The coupling efficiency, η (in dB) can be calculated as:

$$\eta = P_{out} - (P_{in} - 4) \tag{49}$$

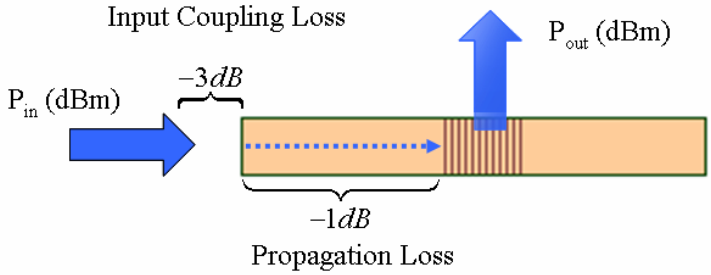

Figure 44 Power losses associated with coupling efficiency measurement

The output coupling efficiency was measured in both directions. When excited from the forward propagation direction, coupling efficiencies as high as ~32% were observed. When excited from the reverse propagation direction, coupling efficiencies as high as ~17% were observed. This is illustrated in Fig. (45). This asymmetric behavior in the coupling efficiencies is expected due to the asymmetric nature of the gratings.

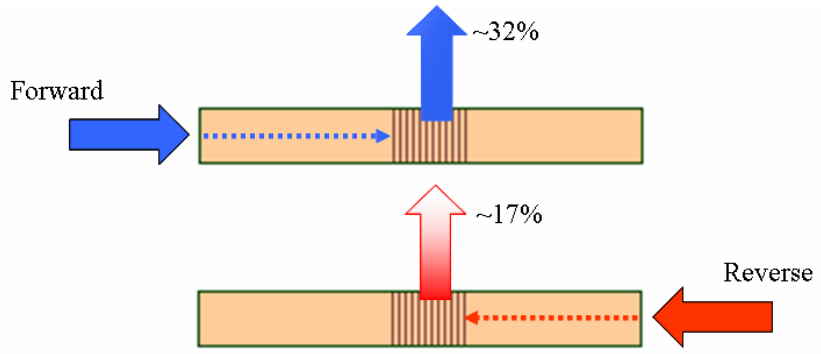

Figure 45 Coupling efficiency for forward and reverse directions

5.3.7 Output coupling efficiency calculation

Tamir and Peng have derived an approximation for the calculation of the output coupling efficiency from a slab waveguide for various grating shapes and periods [23]. A calculation was performed based on their work for a slab waveguide with the same vertical dimensions and indices as the waveguide design shown in Fig. (37). The calculated coupling efficiency is shown in Fig. (46). In the graph the x axis is unit-less and consists of the ratio of the grating height or thickness to the wavelength of the light source. Target ranges for the grating depth to wavelength ratio were on the order of a 0.5 and error ranges of 0.4 to 0.6 have been selected and are represented by the vertical dashed lines. The y axis represents the output coupling efficiency percentage per unit length of the gratings along the direction of the grating period, and is known as the "efficiency to cover". The measured coupling efficiency for the fabricated gratings was 32%. Since the length of the gratings can be anywhere in the range of 125 to 175 μm due to the coherence issues of the laser discussed in section 4.2.4, the measured efficiency to cover is then in the range of .18 to .26. This range is represented on the graph as the two horizontal dashed lines. When compared to the theoretical coupling efficiency a region of interest marked by the shading is

formed. The region shows good agreement between the measured and theoretical data.

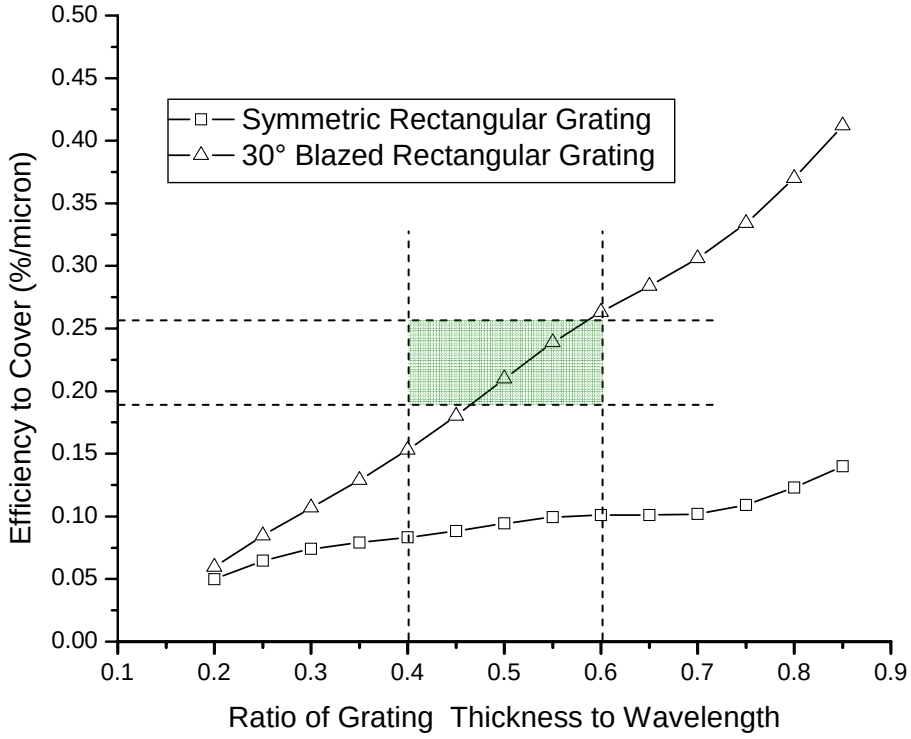

Figure 46 Output coupling efficiency from slab waveguide.

Chapter 6: Chapter summaries, suggested future work and conclusions

6.1 Chapter Summaries

6.1.1 Chapter 2 summary

Starting with the Fresnel-Kirchoff diffraction formula, the equations for diffraction in the Fraunhofer limit have been derived. In addition, equations have been derived for an array of N diffractive elements. An exact solution was found for the diffraction of an array of N periodic 1-D slits of arbitrary width from which a basic understanding of the nature for grating diffraction theory can be obtained. The grating equation was next derived. Lastly, the Fourier approach was discussed, which can be used for grating analysis allowing very simple numerical solutions to be designed using existing well known numerical techniques all ready available for generic Fourier analysis.

6.1.2 Chapter 3 summary

BCB with its excellent chemical resistance and its ability to integrate with existing semiconductor technologies make it an ideal choice for use in integrated photonics applications. In addition, its high absorption at UV wavelengths makes this polymer an ideal choice for laser fabrication via UV sources. Overall making this polymer an excellent candidate for test and development of direct laser fabrication techniques of integrated polymer optic devices.

6.1.3 Chapter 4 summary

A setup for the direct laser fabrication of diffraction gratings on polymer films has been described and implemented. The laser fabrication system offers tremendous time and cost savings when compared to existing lithographic fabrication techniques and allows for rapid prototyping of new grating design parameters. Gratings with periods on the order of .3 to 3 μm have been produced. In addition we have demonstrated a way to produce both symmetrical and blazed diffraction gratings.

6.1.4 Chapter 5 summary

Diffraction gratings have been characterized experimentally and theoretically. Experiments were carried out to determine their transmission characteristics and optimal blazing parameters have been determined. Basic input coupling was demonstrated on multimode polymer dispensed waveguides. The gratings were also used as output couplers from single-mode polymer waveguides and coupling efficiencies as high as 32% have been observed. These output coupling measurements have also been compared to a theoretical model and are in good agreement.

6.2 Suggested future and ongoing work

6.2.1 Single-mode waveguide input coupling efficiency measurement

While input coupling via gratings has been demonstrated on multi-mode waveguides there exists a need to determine and characterize the input coupling efficiency for gratings on single-mode waveguides. However, unlike the multimode

waveguide, rather than a band or range of acceptance angles there will exist only a single input acceptance angle. Because of this and the size of the input coupler, extremely strict tolerances will exist on the input acceptance angle making it very difficult to excite the waveguide. In general end fire coupling into a single mode waveguide requires tolerances along the x and y axis on the order of 1/10 of a micron. For input coupling via a grating there would then additionally need to be a way to vary the angle of the sample in reference to the incoming source to within similar tolerances. A custom alignment system would need to be designed and fabricated to accomplish such a task.

6.2.2 Fabrication on different materials

Grating fabrication for this work was primarily carried out on BCB. However, this fabrication procedure can easily be applied to any polymer or general material which has a high absorption at UV wavelengths. In addition to BCB, work is also being done with materials such as Pyralin and various polymers from Norland Corporation. In addition many other polymers which exhibit nonlinear properties are currently under study and should be considered candidates for laser fabrication.

6.3 Conclusions

With the increasing interest in polymer integrated optical devices, techniques for fabrication of efficient polymer diffraction gratings are of critical importance to aid in coupling of light into and out of polymer waveguides [8-3]. This thesis has proposed and demonstrated a process for the laser fabrication of diffraction gratings. Gratings with various periods have been fabricated and characterized on BCB

polymer thin films. In addition these gratings have been fabricated on dispensed multimode polymer waveguides for use as input couplers and on single mode lithographically fabricated single-mode waveguides for use as output couplers.

With its huge time and cost savings over conventional fabrication of gratings via lithographic techniques, laser fabrication promises to continue to be a very important resource for prototyping and fabrication in the future.

Appendix I. Matlab Source Code

A1.1 Simple calculation of interference pattern

```
clear

%Period of phase mask
LambdaPM = 6.666e-6;
%Desired grating period...not used for this simulation
LambdaG = 1e-6;
%Number of laser modes to calculate
Modes = 4;

%Actual wavelengths of modes
lambdafix = [0.19315e-6  0.19335e-6 0.19355e-6 0.19375e-6]';
%Lens focal length for each mode
foclength = [0.1134295 0.1136030 0.1134874 0.1135453]';

%Multiplied by the period of phase mask determines size of x axis
a=400;
%Number of data points
Nx=2 * a *100 + 1;
xstart  = LambdaPM*a;
x=linspace(-xstart,xstart,Nx);

%Create super gaussian profile input beam
EAmp = exp(-(x*10e2).^(12));

%Calculate distance from phase mask to lens for desired grating period
d =  (LambdaPM/(2*LambdaG) + 1) * foclength(1)

%Calculate angle of for each mode to interfere at
theta = asin((1-d./foclength).*(-lambdafix/LambdaPM));

%Calculate phase for each mode
for n = 1:Modes
   E1(n,:) = EAmp.*exp(-i*2*pi/lambdafix(n)*x*sin(theta(n)));
   E2(n,:) = EAmp.*exp(+i*2*pi/lambdafix(n)*x*sin(theta(n)));
end

%Sum Modes
Output = zeros(1,Nx);
for n = 1:Modes
   Output = Output + abs(E1(n,:) + E2(n,:)).^2;
end
Output = Output / max(Output);
%Graph
figure(1);
plot(x,Output)
```

A1.2 Accurate calculation of interference pattern

```
clear;

%Enable or disable graphs, if =1 then figure is displayed
figure1 = 0;
figure2 = 0;
figure3 = 0;
figure4 = 0;
figure5 = 0;
```

```
figure6 = 0;
figure7 = 1;
figure8 = 0;

%Base wavelength of laser
lambda = 193e-9;
%Period of phase mask
LambdaPM = 6.666e-6;
%Desired grating period...not used for this simulation
LambdaG = 1e-6;
%Number of laser modes to calculate
Modes = 4;

%Actual wavelengths of modes
lambdafix = [0.19315e-6  0.19335e-6 0.19355e-6 0.19375e-6]';
%Lens focal length for each mode
foclength = [0.1134295 0.1136030 0.1134874 0.1135453]';
%Index of lens material for each mode
index = [1.560525  1.560238 1.559953 1.559668]';

%Distance from phase mask to lens roughly calculated as
%(lambdaPM/(2*lambdaG) + 1) * foclength
objdistance = 0.465;

%Distance from lens to sample roughly calculated as
%((2*lambdaG)/LambdaPM +1) * foclength
imgdistance = .1447;

%Multiplied by the period of phase mask determines size of x axis
a=4000;
%Number of data points
Nx=2 * a *100 + 1;

xstart  = LambdaPM*a;
x=linspace(-xstart,xstart,Nx);
dx = 2*xstart / (Nx-1);

%Create super gaussian profile input beam
EAmp = exp(-(x*10e2).^(12));

%%%%%%%%%%%%%%%%%%%%%%%%%%%%%%%%%%%%%%%%%%%%%%%%%%%%%%%%%%%%%%%%%%%%%%%%%%%%%%%
%Ampolitude grating
%%%%%%%%%%%%%%%%%%%%%%%%%%%%%%%%%%%%%%%%%%%%%%%%%%%%%%%%%%%%%%%%%%%%%%%%%%%%%%%
for n = 1 : floor(LambdaPM/dx): Nx - floor(LambdaPM/dx/2)
   for m = 0:floor(LambdaPM/dx/2)
      EAmp(n+m) = 0;
   end
end
if figure1 ==1
   figure(1)
   plot(x,EAmp)
end

%%%%%%%%%%%%%%%%%%%%%%%%%%%%%%%%%%%%%%%%%%%%%%%%%%%%%%%%%%%%%%%%%%%%%%%%%%%%%%%
%Dispersion relation
%%%%%%%%%%%%%%%%%%%%%%%%%%%%%%%%%%%%%%%%%%%%%%%%%%%%%%%%%%%%%%%%%%%%%%%%%%%%%%%
K = 2*pi./lambdafix;
kx=(pi/xstart)*(-(Nx-1)/2:(Nx-1)/2);
for n=1:Modes
   kz(n,:)=sqrt(K(n).*K(n)-kx.^2);
end


%%%%%%%%%%%%%%%%%%%%%%%%%%%%%%%%%%%%%%%%%%%%%%%%%%%%%%%%%%%%%%%%%%%%%%%%%%%%%%%
%Filter out higher orders and propogate
%%%%%%%%%%%%%%%%%%%%%%%%%%%%%%%%%%%%%%%%%%%%%%%%%%%%%%%%%%%%%%%%%%%%%%%%%%%%%%%
FE=fftshift(fft(EAmp));

if figure2 == 1
   figure(2)
```

```
   plot(abs(FE).^2)
end

%Filter out orders >= |1| and 0
filter = zeros(1,Nx);
filter((Nx-1)/2 - 2*a - a:(Nx-1)/2 - 2*a + a) = 1;
filter((Nx-1)/2 + 2*a - a:(Nx-1)/2 + 2*a + a) = 1;
FE = filter.*FE;
if figure3 == 1
   figure(3)
   plot(abs(FE).^2)
end

if figure4 ==1
   figure(4)
   plot(abs(FE).^2)
end

%Propogate from gratings to lens
for n = 1:Modes
   FEProp(n,:)=FE.*exp(i*(kz(n,:))*objdistance);
end
if figure5 == 1
   figure(5)
   plot(abs(FEProp(1,:)).^2)
end

for n = 1:Modes
   FEProp(n,:)=fftshift(FEProp(n,:));
   NewE(n,:)=ifft(FEProp(n,:));
end

if figure6 ==1
   figure(6)
   plot(x,abs(NewE(1,:)).^2)
end

%%%
```

```
    plot(x,Output);
    axis([-5e-4 5e-4 0 1]);
end
%Display 6 Periods
if figure8 == 1
    figure(8);
    plot(x,Output);
    axis([ -3e-6 3e-6 0 1]);
end
```

A1.3 Grating transmission diffraction efficiency

```
clear;

%number of data points in one period
d = 100;

%number of periods
N = 150;

%Amount to oversample for frequency spectrum
foversample = 100;

%Wavelength of illumination source (meters)
lambda = .632e-6;

%Grating period (meters)
lamdag = 2.3e-6;

%Grating depth (meters)
gdepth = .4e-6;

%Index of grating material
n=1.55;


%%%%%%%%%%%%%%%%%%%%%%%%%%%%%%%%%%%%%%%%%%%%%%%%%%%%%%%%%%%%%%%%%
%Transfer function
%%%%%%%%%%%%%%%%%%%%%%%%%%%%%%%%%%%%%%%%%%%%%%%%%%%%%%%%%%%%%%%%%
t = zeros(1,d);
K = 2*pi/lambda;

for l = 0:d:(N - 1)*d
    for m = 1:1:d

        %Grating shape
        gx = (cos(2*pi*(m-1)/d)+1)/2;

        t(l+m) = exp(i*K*gdepth*(1-n)*gx);
    end
end

%%%%%%%%%%%%%%%%%%%%%%%%%%%%%%%%%%%%%%%%%%%%%%%%%%%%%%%%%%%%%%%%%
%Determine range of valid data points in frequency domain
%%%%%%%%%%%%%%%%%%%%%%%%%%%%%%%%%%%%%%%%%%%%%%%%%%%%%%%%%%%%%%%%%
fsamples = d * foversample;
dx = lamdag/d;
f = 1/dx;
fspectrum = -f/2:f/fsamples:f/2 - f/fsamples;
fangularspectrum = asin(fspectrum* lambda/1.55) * 360 / (2*pi);

upperlimit=0;
lowerlimit=0;
for m = 1:1:fsamples
    if real(fangularspectrum(m)) > -89.99999999
        if lowerlimit == 0
            lowerlimit=m;
        end
    end
```

```
    if real(fangularspectrum(m))>89.9999999 && lowerlimit ~= 0
        if upperlimit == 0
            upperlimit=m-1;
        end
    end
end

%%%%%%%%%%%%%%%%%%%%%%%%%%%%%%%%%%%%%%%%%%%%%%%%%%%%%%%%%%%%%%%%%%%%%%%
%Calculate Fourier transform of transfer function
%%%%%%%%%%%%%%%%%%%%%%%%%%%%%%%%%%%%%%%%%%%%%%%%%%%%%%%%%%%%%%%%%%%%%%%
T = fftshift(fft(t,fsamples));
MagT = abs(T).^2;
MagT = MagT/max(MagT);
figure(1);
plot(fangularspectrum(:,lowerlimit:upperlimit),MagT(:,lowerlimit:upperlimit))
```

References

[1] A. Chen, V. Chuyanov, S. Carner, W. H. Steier, J. Chen, Y. Ra, S. Mao, L. Guo and L. R. Dalton, "Fast maskless fabrication of electrooptic polymer devices by simultaneous direct writing and electric poling of channel waveguides", LEOS '97 10th Annual Meeting. Conference Proceedings., IEEE , Volume: 2 , 10-13 Nov 1997, 250 -251 vol.2 (1997).

[2] R. Waldhausl, B. Schnabel, E.-B. Kley and A. Brauer, "Efficient focusing polymer waveguide grating couplers", Electronics letters, 33, 623-624 (1997).

[3] S. Ura, M. Shinohara, T. Suhara and H. Nishihara "Integrated-optic grating-scale-displacement sensor using linearly focusing grating couplers", IEEE Photo. Tech. Lett., **6,** 239-241 (1994).

[4] G. Hutchinson, Y. Kim, W. Cao, Y. Leng, V. Yun, L. Lucas, C.H. Lee, W.N. Herman, and J. Goldhar, "Direct Laser fabrication of blazed diffraction coupling gratings on single mode polymer waveguides", *ACS National Meeting* 2004 *Organic Thin Film Symposium,* paper PMSE 201, (Philadelphia, PA).

[5] G. P. Behrmann and M. T. Duignan, "Excimer laser micromachining for rapid fabrication of diffractive optical elements," Applied Optics, vol. 36, pp. 4666-4674, (1997).

[6] T.W. Mossberg, C.M. Greiner, D. Iazikov, *Laser Focus World*, vol. 40, pp. 73-76, (2004).

[7] Y. Leng, V. Yun, G. Hutchinson, M. Du, C. H. Lee, W. N. Herman, J. Goldhar, "Direct laser fabrication of optical polymer waveguides and Bragg grating couplers," *OSA Annual Meeting 2003 Organic Thin Film Symposium*, poster MT114, (Tucson, AZ).

[8] K. Chen, J. Ihlemann, P. Simon, I. Baumann, W. Sohler, "Generation of submicron surface gratings on $LiNbO_3$ by ultrashort UV laser pulses," *Appl. Phys. A*, vol. 65, pp. 517–518, (1997).

[9] K.O. Hill, B. Malo, F. Bilodeau, D.C. Johnson, "Bragg gratings fabricated in monomode photosensitive optical fiber by UV exposure through a phase mask," *Applied Physics Letters*, vol. 62, pp. p. 1035-1037, (1993).

[10] P.E. Dyer, R.J. Farley, R. Giedl, C. Ragdale, "Study and analysis of submicron-period grating formation on polymers ablated using a KrF laser irradiated phase mask," *Applied Physics Letters,* vol. 64, pp. 3389-91 (1994).

[11] P. E. Dyer, R. J. Farley, R. Giedl, and D. M. Karnakis, "Excimer laser ablation of polymers and glasses for grating fabrication," *Appl. Surf. Sci.,* vol. 96-98, pp. 537-549, (1996).

[12] K.J. Ilcisin, R. Fedosejevs, "Direct production of gratings on plastic substrates using 248-nm KrF laser radiation," *Applied Optics*, vol. 26, pp. 396-400 (1987).

[13] T. Lippert, Gerber, A. Wokaun, D.J. Funk, "Single pulse nm-size grating formation in polymers using laser ablation with an irradiation wavelength of 355 nm," *Applied Physics Letters*, vol. 75, pp. 1018-1020, (1999).

[14] M. Born and E. Wolf, "*Principles of Optics – 7th ed.*," Cambridge University Press, Cambridge, UK, (1999).

[15] Goodman, J., *"Introduction to Fourier Optics,"* McGraw-Hill , 1996.,

[16] C. R. Pollock, "Fundamentals of Optoelectronics," Richard D. Irwin, Inc., (1995).

[17] A. Yariv, "*Optical Electronics in Modern Communications – 5th ed.*," Oxford University Press, New York, NY, (1997).

[18] The Dow Chemical Company. Cyclotene: Advanced Electronic Resins. [Online] Available http://www.cyclotene.com, October 1, (2004).

[19] D. Derickson, "Fiber Optic Test and Measurement," Prentice-Hall, Inc, Upper Saddle River, New Jersey, (1998).

[20] R. G. Adams and M. M. Dillon, *J. Appl. Phys*., Vol. 70, No. 8, (1991).

[21] V. Yun, Y. Leng, D. Weinstein, L. Lucas, W. Herman, C. Lee and J. Goldhar, "Direct dispensing polymer waveguides for Photonic Device Integration," *ACS National Meeting* 2004 *Organic Thin Film Symposium,* paper PMSE, (Philadelphia, PA).

[22] J. Witzens, A. Scherer, G. D. Pickrell, Louderback, P. Guilfoyle, "Monolithic integration of vertical-cavity surface-emitting lasers with in-plane waveguides," *Applied Physics Letters*, vol. 86, pp. 101105-101115, (2005).

[23] S. Zhang and T. Tamir, *"Analysis and design of broadband grating couplers,"* IEEE J. Quantum Electronics, vol. 29, pp. 2813-2824, (1993).